Atomization of Viscous Fluids using Counterflow Nozzle

A THESIS
SUBMITTED TO THE FACULTY OF THE GRADUATE SCHOOL
OF THE UNIVERSITY OF MINNESOTA
BY

Roshan Rangarajan

IN PARTIAL FULFILLMENT OF THE REQUIREMENTS
FOR THE DEGREE OF
MASTER OF SCIENCE

Prof.Vinod Srinivasan

August, 2020

© Roshan Rangarajan 2020
ALL RIGHTS RESERVED

Acknowledgements

I would like to express my sincere gratitude to my academic advisor, Prof.V.Srinivasan for his continuous support throughout this pursuit. His consistent motivation guided me during the course of this rigorous experimental effort. He helped instill a deep sense of work ethic and discipline towards academic research.

In addition, I would like to thank Prof.Strykowski (ME Dept, University of Minnesota-Twin Cities) and Prof.Hoxie (ME Dept, University of Minnesota-Duluth) for their engaging technical insights into my present work. In particular, I was able to develop a sound understanding of techniques used in Image processing through my interactions with Eric and Prof.Hoxie at UMN-Duluth.

I would like to thank my fellow lab mates Akash, Ian, Chinmayi, Manish, Sankar, Ankit, Peter and Amber for simulating discussions and sleepless nights before important deadlines. Research becomes not just interesting but also fun when you have the right minds around.

Besides my advisor, I would like to thank Prof.Hogan and Prof.Ramaswamy for their time and encouragement in this work.

Dedication

Parents and my sister for always believing in me.

Abstract

In the present work, we study the enhanced atomization of viscous liquids by using a novel twin-fluid atomizer. A two-phase mixing region is developed within the nozzle using counterflow configuration by supplying air and liquid streams in opposite directions. Detailed qualitative and quantitative measurements for droplet size were conducted using shadowgraph technique. Near-field spray images from the nozzle exit suggest that the spray emerges out as a fine droplets with little scope for further atomization. The performance of this nozzle is compared to the 'flow-blurring' nozzle. Three test liquids (Water, Propylene Glycol & Glycerol 85% soln) are used to vary the liquid viscosity in the range from 1 to 133.5 mPa.s. The counterflow nozzle produces a spray whose characteristics are relatively insensitive to fluid viscosity over the range of gas-liquid mass flow ratios between 0.25 and 1.

Nomenclature

Table 1: Nomenclature for variables used in the present work

Symbol	Meaning
A	Spray surface area[m^2]
d32	Sauter mean diameter[m]
d0	Nozzle exit diameter [m]
d1	Outer diameter of exit tube [m]
d2	Inner diameter of outer tube of nozzle [m]
D	Exit diameter of flow-blurring nozzle [m]
g	Annular gap between liquid tube and housing [m]
CF	Counterflow
FB	Flow Blurring
ALR(β)	Air to Liquid Ratio
r	Radial distance [mm]
z	Downstream distance [mm]
ρ	Density of fluid [kg/m^3]
σ	Surface tension of fluid [N/m]
μ	Viscosity of fluid [Pa.s]
η	Nozzle Efficiency
Re	Reynolds Number
Oh	Ohnesorge Number
We	Weber Number
$\dot{m}$	mass flow rate
Subscript	
l	Liquid
a	Air

Contents

List of Tables

List of Figures

Chapter 1

Introduction

The present work examines the effect of viscosity on the atomization performance of a counterflow nozzle. For this experimental investigation, a custom rig using the shadowgraph technique is used. The overall goal is to study the performance of counterflow nozzles under varying conditions and then to document the comparison with other nozzle types that have been studied in the literature. The breakup of bulk liquid into smaller particles finds use in a wide range of industrial applications such as combustion, food processing, pesticide and drug delivery. Atomization is an inherently complex transient process that has been studied for over 50 years. The present undertaking is motivated by the desire to add to this base of knowledge, by including the less understood influence of viscosity on performance of counter-flow nozzle.

Atomization process involves disintegration of liquid into drops by the acting forces[3]. This additional energy is used in increasing the surface energy of the resulting mist of droplets. One of the several means of achieving this is by using kinetic energy of air in twin-fluid atomisers. As discussed earlier, the performance of counterflow nozzle is documented in the present work against 'flow-blurring' nozzle which will be introduced to the readers in the next chapter.

There is growing industrial demand to obtain controlled size distributions in sprays in order to correlate this information with broad range of applications. For example, important combustion characteristics such as ignition and volumetric heat release depend upon the droplet spectrum. For evaporative cooling application, drop surface area is needed to estimate the heat and mass transfer. In case of agricultural spraying of

pesticide, drop drift and coverage is influenced by drop size and similar analogy could be made for spray painting and other coating applications [3].

Chapter 2 presents a overview on atomization. The review includes a brief introduction to the liquid break up before proceeding to explain different aspects of twin fluid atomization. We discuss different internal nozzle flow configurations described in literature.

Chapter 3 presents the primary objective of the present work. An experimental matrix is laid out to the reader for achieving this objective.

Chapter 4 describes the experimental setup in greater detail. The experimental procedure and troubleshooting measures taken to ensure consistent results have been discussed in the subsequent sections.

Chapter 5 begins with analysis procedure used to extract useful information from the raw data sets. Subsequent sections are used to describe qualitative and quantitative results obtained in this study.

Chapter 6 draws on the previously obtained results. Key results have been summarised in this chapter.

Chapter 2

Background

Liquid breakup theory has been studied for the past several decades in an attempt to understand liquid-air interaction at low Reynolds number. This work, however, is focused on atomization of fluids at high Reynolds number. This chapter has been divided into two separate subsections ; Theoretical Background & Experimental Work. Theoretical background chapter deals with liquid breakup theory and offers a high level overview of atomization. Then, we start to take a closer look at twin-fluid atomization in the next sub-section on experimental work. Important non-dimensional numbers are also introduced to the reader through technical discussion. The summary of work embodied in this section is by no means exhaustive and is presented to provide a means of motivation for the current study.

2.1 Theoretical Background

The literature on the theory of liquid breakup is fairly extensive but primarily deals with low-velocity discharge of liquid from nozzle exit. This, though useful in identifying fundamental physics behind liquid breakup, is not extremely relevant from an application stand point. There is no single theory which could answer the fundamental question – what spectrum of droplets will be obtained under a particular set of conditions? This is due to the highly complex and transient phenomena that occurs during atomization.

Early Works : Rayleigh's early work [24][25][31][30] involving breakup of non-viscous liquid breakup laid the foundation for this field. He showed that the jet breakup

is a consequence of hydrodynamic instability. The most unstable wavelength was shown to be 143.7% of jet's circumference[21]. He later investigated the effect of viscosity on the disturbance growth rate. Chandrasekhar [4] extended Rayleigh's work and accounted for effects of liquid density and viscosity. He showed that viscosity tends to reduce the breakup rate and increase droplet size. Taylor [34] included the effect of ambient gas density in his analysis.

Jet Breakup : Jet breakup phenomena could be divided into different regimes based upon the level of interaction between the liquid jet and the ambient gas. Major breakup regimes are identified in the Fig 2.1 by Lin & Reitz ([21]). Coherent portion of the liquid jet, L is shown as a function of jet exit velocity, U to characterise the different jet breakup regimes. Increasing velocity beyond dripping regime shows a linear relation between jet velocity and breakup length until it reaches a maxima (Region A & B). Droplets that begin to pinch off from the core jet of liquid have diameters comparable to the diameter of the jet itself. These first two regimes: Rayleigh and first order wind-induced regime are reasonably well understood using linear stability theory. Further attempts to model the shape of this breakup curve and point of exact location for maximum breakup length have disagreements with experimental data[21][13].

Effect of Fluid parameters : From the earlier discussion, it's clear that the disintegration of a liquid jet is promoted by turbulence in liquid jet and by the action of aerodynamic forces on the surface of the jet. These two forces are opposed by the viscosity and surface tension forces of the liquid, which tend to preserve the continuous and compact state of the liquid jet. To some extent this argument can be generalised by stating that the degree of atomization will be improved if the action of the first two factors (i.e.turbulence and air forces) be increased, and if the latter two (i.e.liquid viscosity and surface tension) be reduced [11] .

Let us consider the different stages of liquid atomization process and understand the influence of liquid properties at each stage. Firstly, let's look at the continuous liquid jet that emerges out of an atomiser. Higher the viscoisty of the jet, lower will be the tendency of the jet to disintegrate. Hence, in this stage, the effect of viscosity is dominant.

After emerging out of the nozzle, the jet will form thin layer of liquids near the interface known as ligaments which further break into separate droplets. Most of the

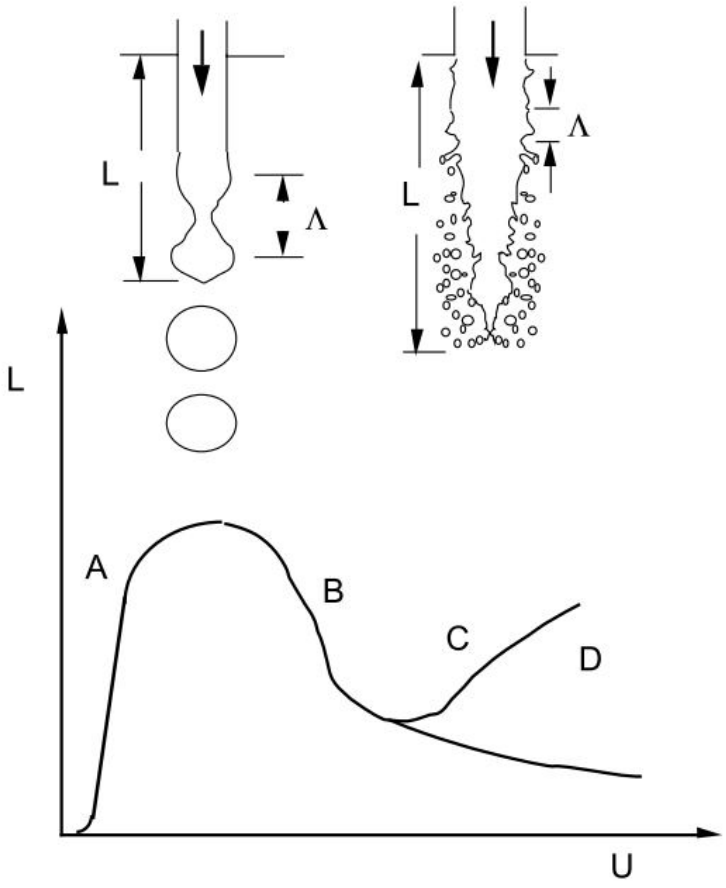

Figure 2.1: Jet Breakup length as a function of liquid velocity [21]

interesting dynamics in this secondary stage of atomization occurs at the the interface. Hence, the effect of surface tension becomes important for fundamental mechanism driving this ligament breakup.

The next and final stage of atomization is the subdivision of already formed droplets as they move through the surrounding medium. This breakup depends upon the relative magnitude of inertial,surface tension and viscous forces on one hand to aerodynamic forces on the other. This criteria is defined by the droplet Weber Number as shown in Eqn 2.3. The droplets that have lower surface tension & have high discharge velocity would split up more readily at higher Weber numbers. On the other hand, viscosity increases the time the droplet takes to sufficiently deform to undergo subdivision, thereby

preventing it the droplet to attain critical velocity for breakup. Overall, all the three liquid parameters (surface tension, liquid viscosity & specific gravity) play a key role in this final stage of atomization. [11].

Non-Dimensional Numbers : In order to scale experimental results, several important non-dimensional numbers are defined. Air to Liquid Ratio (ALR or β) shown in Eqn 2.1 is defined as the ratio of mass flow rate of air to mass flow rate of liquid through the nozzle. Ohnesorge number(Oh) shown in Eqn 2.2 is the ratio of fluid's viscous forces to inertial and surface tension forces. Webern umber(We) shown in Eqn 2.3 is the ratio of fluid's inertial force to it's surface tension force. Reynolds number (Re) shown in Eqn 2.4 is the ratio of fluid's inertial force to it's viscous forces.

$$ALR = \beta = \frac{\dot{m}_a}{\dot{m}_l} \tag{2.1}$$

$$Oh = \frac{\mu}{\sqrt{\rho \sigma L}} \tag{2.2}$$

$$We = \frac{\rho v^2 l}{\sigma} \tag{2.3}$$

$$Re = \frac{\rho v D}{\mu} \tag{2.4}$$

Atomization quality: The drops within a spray have a large scatter of diameters (polydisperse). Usually, this scatter is undesirable but obtaining an approximately uniform drop distribution is very difficult. In order to quantity this large distribution, Sauter Mean Diameter (SMD or d_{32}) is often used to describe spray quality in atomization literature.

$$D_{32} = SMD = \frac{\sum nD^3}{\sum nD^2} \tag{2.5}$$

SMD is the diameter of a uniform equivalent droplet set with the same volume to surface area of all droplets (n) in the real set. In order to obtain an accurate representation of the data set, drop sizing techniques should have large sample size. The relationship between accuracy of determination of SMD and sample size has been shown in Table 2.1.

Number of drops	Accuracy (%)
500	± 17
1400	± 10
5500	± 5
35000	± 2

Table 2.1: Accuracy of determination of SMD as a function of quantity of drops measured [2]

Nozzle Efficiency: The energy E supplied to the atomizer is given by [3]:

$$E = E_A + E_K + E_L \tag{2.6}$$

where E_A = energy of atomization (energy used to overcome surface tension)
E_K = kinetic energy (energy used to set the liquid in motion)
E_K = Energy loss (energy used to overcome the frictional forces in the atomizer)

$$\eta = \frac{E_A}{E} \tag{2.7}$$

$$\eta = \frac{\sigma A}{\dot{m}_l \Delta h_l + \dot{m}_a \Delta h_a} \approx \frac{6\sigma\rho_a}{\beta \Delta p_a d_{32} \rho_l} \tag{2.8}$$

Efficiency η is defined as the ratio of the energy E_A used for the development of a new liquid surface(surface of drops) to the total energy used in this process as shown in Eqn 2.7. In case of twin fluid pneumatic nozzle, this energy is supplied by the change in enthalpy of the two fluids. Rearranging the terms, and using β as the Air-Liquid ratio, σ as the surface tension between liquid & air, ρ as the density of fluid, Δp_a as the air pressure drop,d_{32} as Sauter mean diameter; we obtain a simplified expression in Eqn 2.8 for nozzle efficiency in measurable terms as later discussed in the experimental section.

2.2 Twin-fluid Atomization

The reader has been introduced to several important atomization concepts and non-dimensional numbers in section 2.1. Efficiency Eqn 2.8 introduces the concept of twin fluid atomization. In this work, we concentrate mainly on the use of twin-fluid atomization of viscous liquids using different atomizer designs. Pressure atomizer described

earlier, use a high velocity liquid jet to spray into quiescent environment. The aerodynamic forces resulting from velocity differences in the 2-fluid stream cause instability to grow at the interface leading to primary breakup. Using a similar principle, twin fluid atomizers deploy impingement of high velocity gas stream into low velocity liquid stream. Twin fluid configuration offers better atomization of higher viscous fluids even at low flow rates as compared to a pressure atomizer [20].

Primary Breakup : Most of the discussion in this section would be on cylindrical liquid jet by an annular high velocity gas stream. Both fluids are assumed to be flowing in the same direction as conventionally defined as co-axial air assist atomisation. Chigier et al reported a extensive experimental investigation on coaxial air-water jets [5][6][7][8]. Farago & Chigier [5] proposed a classification of disintegration of coaxial air-water jets. They identified 3 atomization regimes : The Rayleigh-type breakup, the Membrane type breakup and the fiber-type breakup was based on relative gaseous Weber Number (We_R). U_G,U_L,d_L stand for gas stream velocity, liquid stream velocity and orifice diameter respectively.

$$We_R = \frac{\rho_G (U_G - U_L)^2 d_L}{\sigma} \tag{2.9}$$

The investigation was carried out for a range of We_R from 0.001 to 600. Rayleigh type breakup occurs when the droplets of the order of jet diameter pinch off from the core liquid without any kind of membrane/ligament formation. This regime could be further divided : (a) Axisymmetric subregime ($We_R < 15$) (b) Non-axisymmetric sub regime ($15 < We_R < 25$) . The breakup length is shorter than a liquid jet into a still environment that was discussed previously. The hook-like liquid jet breakup at lower Weber number can be seen in Fig 2.2 (a). Membrane type breakup ($25 < We_R < 70$) shown in Fig2.2(b) is characterised by the development of thin liquid sheet due to Kelvin-Helmholtz waves and breaks into droplets of much smaller diameter than the jet diameter. The fiber-type regime ($100 < We_R < 500$) depicted in Fig2.2(c) shows liquid fibers from ligaments shedding off the jet. The diameters of the resulting droplets are very small and typically undergo secondary atomization discussed in the next section. Farago & Chigier further divided this regime into 2 sub-modes :pulsating and superpulsating modes. The defined the criteria for superpulsating mode as :

$$\frac{Re_L}{We_R^{0.5}} < 100 \tag{2.10}$$

Superpulsating sprays are subjected to high periodic changes in low high density regions in the sprays.

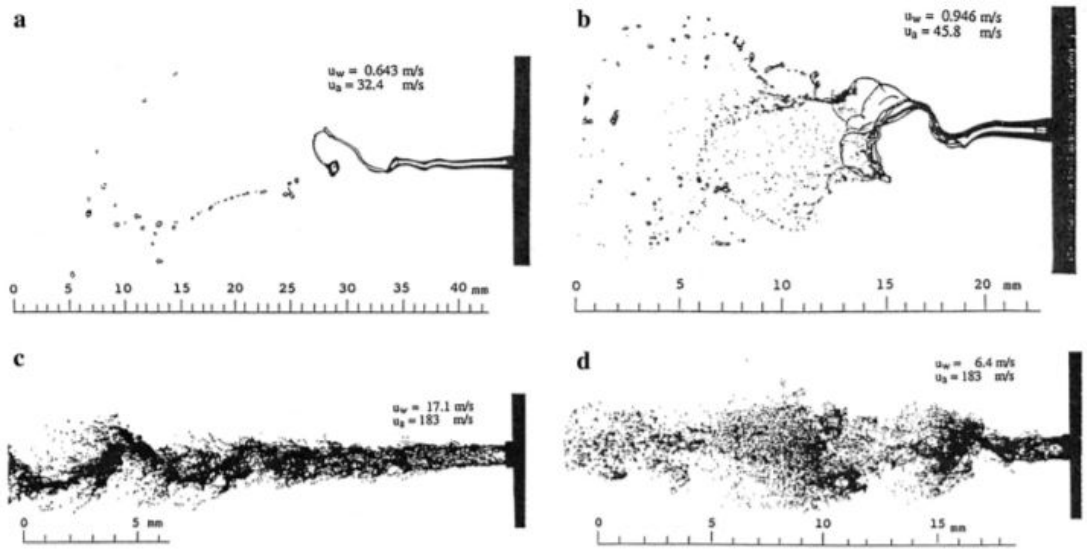

Figure 2.2: Air-assisted cylindrical jet atomization regimes. (a) Non-axisymmetric Rayleigh regime (b) membrane-type regime (c) fiber-type regime(d) superpulsating submode [5]

Secondary Breakup : The secondary breakup process starts when the drop experiences a disruptive flow field and undergoes deformation phase. The deformation of a spherical droplet subject to unequal pressure distribution, is opposed by viscous and surface tension forces as discussed earlier. However, if the dynamic pressure acting on the droplet is larger than the resistive forces, then it would enter the fragmentation phase. This depends upon different flow conditions. An overview of different breakup modes under different flow conditions has been depicted in Fig 2.3. From top to bottom the modes are termed vibrational, bag, multimode (often called bag-and-stamen), sheet-thinning, and catastrophic [12].

Vibrational breakup occurs due to oscillations at the natural frequency and are rarely observed in practical conditions. It results in producing a few droplets that are similar in size to that of the parent drop itself.

The bag mode has a toroidal rim attached to a hollow bag. The bag breaks first with a large number of small droplets followed by the breakup of the rim into a small

number of large droplets.

The multimode (bag & stamen mode) is similar to bag mode with the addition of a stamen in the antiparallel direction to that of droplet motion. It derives it's name from the range of different droplet diameters produced in this mode.

In the sheet thining mode, the droplets are continously peeled off from the parent droplet surface. This results in a large number of small droplets with the occasional appearance of a large droplet having a size comparable to that of the parent droplet.

Catastrophic breakup of the droplet surface occurs due to waves of large amplitude and result in a large number of small droplets. Attempts have been made to classify these different regimes based on non-dimensional numbers such as Weber Number and Ohnesorge number as seen in Table 2.2.

Mode of Breakup	Weber Number
Vibration	$0 < We < 11$
Bag	$11 < We < 35$
Multimode	$35 < We < 80$
Sheet-thinning	$80 < We < 350$
Catastrophic	$We > 350$

Table 2.2: Weber No. Transition for different modes($Oh < 0.1$) [12]

Co-flow Atomiser : Most of the modern day nozzles are based on co-flow configuration. It typically has a low velocity liquid at the core and a low density gas in the annulus. Depending upon where the gas-liquid interact, they are further classified as internal-mixing and external-mixing nozzles. Several attempts have been made to develop a cohesive atomization model to predict and model the performance of co-flow atomizer. One such attempt demonstrated by Varga [35] & Aliseda [1] has been discussed briefly in this section. A schematic 2D sketch is shown in Fig 2.4, where the liquid is flowing at U_{Liquid} velocity in the core & the high velocity gas is flowing coaxially with a velocity U_{Gas}. The difference in velocity between the two liquid streams results in growth of unstable waves at the interface. The final droplet diameter produced by the nozzle is shown to be a strong function of the wavelength corresponding to maximum growth rate in instability.

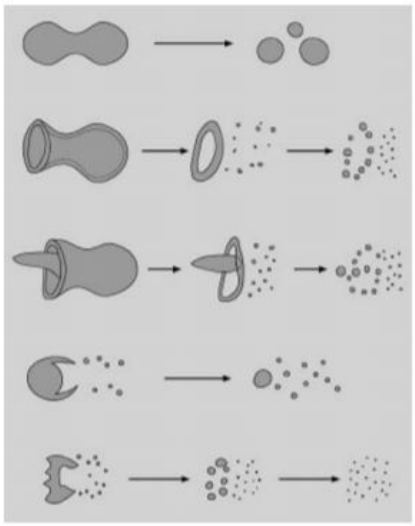

Figure 2.3: Newtonian drop breakup morphology [12]

$$\lambda_1 = 2\delta_g \sqrt{\frac{\rho_l}{\rho_g}} \tag{2.11}$$

$$\delta_g = \frac{Cb_g}{\sqrt{Re_{bg}}} \tag{2.12}$$

$$Re_{bg} = \frac{U_{Gas} b_g}{\nu_{Gas}} \tag{2.13}$$

$$U_c = \frac{\sqrt{\rho_l} U_{Liquid} + \sqrt{\rho_g} U_{Gas}}{\sqrt{\rho_l} + \sqrt{\rho_g}} \tag{2.14}$$

Using dispersion relation suggested by Joseph [16] and assuming high viscosity fluid in the core, we obtain an approximate expression for Rayleigh-Taylor wavelength for maximum growth rate as shown in Eqn 2.15.

$$\lambda_{RT} = \sqrt{\frac{\sigma \lambda_1}{\rho_g (U_g - U_c)^2}} (1 + C_2 (\frac{\rho_g (U_g - U_c)^2}{\lambda_1 \sigma})^{1/6} (\frac{\alpha_1^2}{\sigma \rho_1})^{1/3}) \tag{2.15}$$

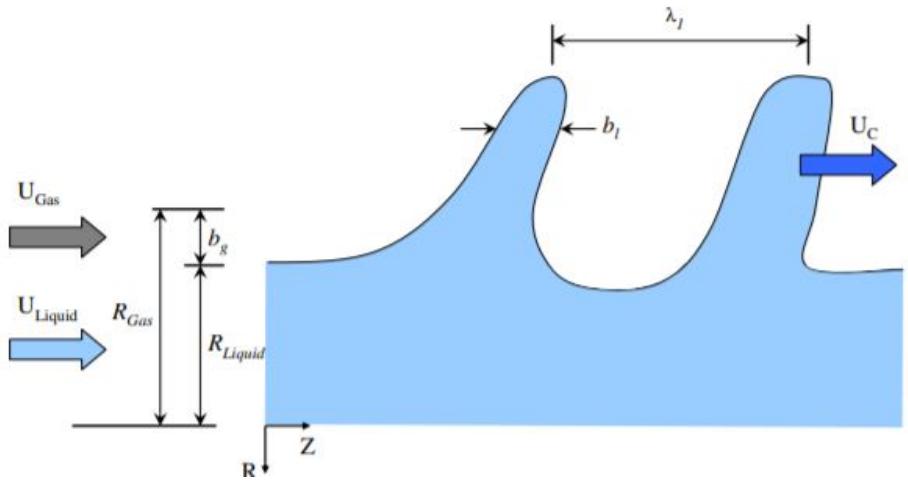

Figure 2.4: Schematic sketch for primary instability in the liquid stream caused by the high-speed, coaxial air stream [1]

Assuming that the drop diameter (SMD) is a fraction of RT Wavelength [35] and using Eqn 2.11, we obtain a final expression for droplet diameter in Eqn 2.16.

$$\frac{SMD}{D_1} = C_1(1+m_r)\sqrt{\frac{b_g}{D_1}}(\frac{\rho_l/\rho_g}{Re_{bg}})^{1/4}\frac{1}{\sqrt{We_{D1}}}(1+C_2(\frac{D_1}{b_g})^{1/6})(\frac{Re_{bg}}{\rho_l/\rho_g})^{1/12}We_{D1}^{1/6}Oh^{2/3} \tag{2.16}$$

Various non-dimensional numbers used in Eqn 2.16 have been defined as follows :

$$We_{D1} = \frac{\rho_g(U_{Gas}-U_c)^2 D_1}{\sigma} \tag{2.17}$$

$$Oh = \frac{\alpha_1}{\sqrt{\rho_l \sigma D_1}} \tag{2.18}$$

$$m_r = \frac{\rho_l U_{Liquid} A_l}{\rho_g U_{Gas} A_g} \tag{2.19}$$

α_1 in Eqn 2.18 refers to the viscosity of the Non-newtonian fluid considered in this study. It's effective viscosity has been taken at the maximum shear rate in order to compute these equations. C_1 & C_2 are constants of the order of unity and depend upon experimental conditions(type of liquid, nozzle geometry). Mass loading $(1+m_r)$ includes

effect of relative size of liquid and air exit into the equation as outlined by Mansour [23]. The model behavior closely match with the experimental results obtained for fluids having significant rheological complexity[35].

Investigators	Air Velocity (U_a)	Air density (ρ_a)	Surface Tension (σ)	Dimesnion (d_0)
Nukiyama and Tanasawa	-1	0	0.5	0
Weiss and Worsham	-1.33	-0.3	-	0.16
Gretzinger and Marshall	-0.40	-0.40	0	-
Kim and Marshall	-1.14	-0.57	0.41	-
Lorenzetto and Lefebvre	-1.00	-0.33	0.3	0
Jasuja	-0.90	-0.45	0.45	0.55
Ingebo	-0.75	-0.25	0.25	0.5

Table 2.3: Summary of data on power dependence of variables on mean drop size for low viscosity fluids [26]

In spite of the large volume of work available on Co-flow atomizers, we still have unanswered questions on the influence of air stream Mach number and liquid stream Reynolds number on spray quality [26]. In the absence of a clear first principle based approach, most of the modeling work uses a combination of non-dimensional analysis for scaling and empirical correlations in order to fit performance data. This has resulted in significant scatter in performance curves among researchers using different atomizer designs and measurement techniques as shown in Table 2.3. Rizk & Lefebvre [26] have developed a droplet diameter prediction model based on flow conditions and fluid properties as shown in Eqn 2.20. This equation would be later used to compare performance of other atomizer configuration with Air-Blast (AB) Atomizer.

$$\frac{SMD}{d_0} = 0.48(\frac{\sigma}{\rho_A U_A^2 d_c})^{0.4}(1+\frac{1}{ALR})^{0.4} + 0.15\sqrt{\frac{\mu_L^2}{\sigma\rho_L d_c}}(1+\frac{1}{ALR}) \tag{2.20}$$

It can be seen that the droplet diameter have been scaled with respect to the exit orifice diameter (d_0). Increasing viscosity and lowering of Air-to-Liquid(ALR) ratio would lead to increase in expected drop mean diameter. Co-flow configuration despite being the industry standard for pneumatic twin-fluid nozzles suffers from significant limitations. In order to produce fine droplets, high air flow rate at higher pressure must be used. This results in increased power requirement for operating the nozzle [19]. It

performs poorly for fluids with higher kinematic viscosity resulting in larger droplets. In case of biofuel combustion, poor atomization results in higher PM, CO and NO_x emissions [27]. Recent research has looked into alternative atomizer configurations to overcome these traditional limitations of a co-flow nozzle.

Effervescent Atomization : This concept shown in Fig 2.5 comprises of a plain-orifice atomizer with means for injecting air (or gas) into the bulk liquid at some point upstream of the injector orifice. This air injection occurs through needle like holes in the aerator tube and occurs at low velocity. The pressure differential between gas and liquid is just enough for gas injection. This results in bubble formation and a complex 2-phase flow at the orifice. The liquid flowing through the injector orifice is squeezed by the surrounding gas bubbles into thin shreds and ligaments. This greatly aids atomization since these ligaments undergo catastrophic secondary breakup resulting in fine droplets near the exit of the nozzle. It is also well established that the droplet size is roughly proportional to the square root of the initial thickness or diameter of the ligaments from which they are formed [20]. The internal flow in an effervescent atomizer is more complex than in most single and twin fluid atomizers, since it involves internal mixing of the liquid with the atomizing gas at low velocity and the rapid evolution of the two-phase mixture as it flows through the atomizer and out through the discharge orifice [29]. Table 2.4 shows a summary on effect of different operating conditions on performance of effervescent atomizer. It is widely accepted across the investigators that liquid viscosity seems to be insignificant in effervescent atomization. The phyics governing the breakup deals with ligaments/thin sheets instead of the bulk fluid and hence the performance is relatively free from influence of viscosity.

Investigators	Pressure difference (ΔP)	Orifice Diameter (D_0)	Liquid Density (ρ_L)	Surface Tension (σ)	Liquid viscosity (μ_L)	ALR
Sojka and Lefebvre, 1990	-1.204	-	-	1	-	-0.0461
Lefebvre, 1992a	-	-	-0.914	0.0239	-	-0.0221
Lefebvre, 1992b	-	1	-0.914	0.0239	-	-0.0221
Lund, 1993	-	-	-0.014	-0.014	0.159	-
Wade et al., 1999	-0.90	-0.93	-	-	-	0.005
Kim and Lee, 2001	0.0062	0.7166	-0.0062	0.4846	-	1

Table 2.4: Influence of operating parameters on SMD correlations proposed by various researchers [17]

The performance of effervescent atomizer is extremely good at very low ALRs and

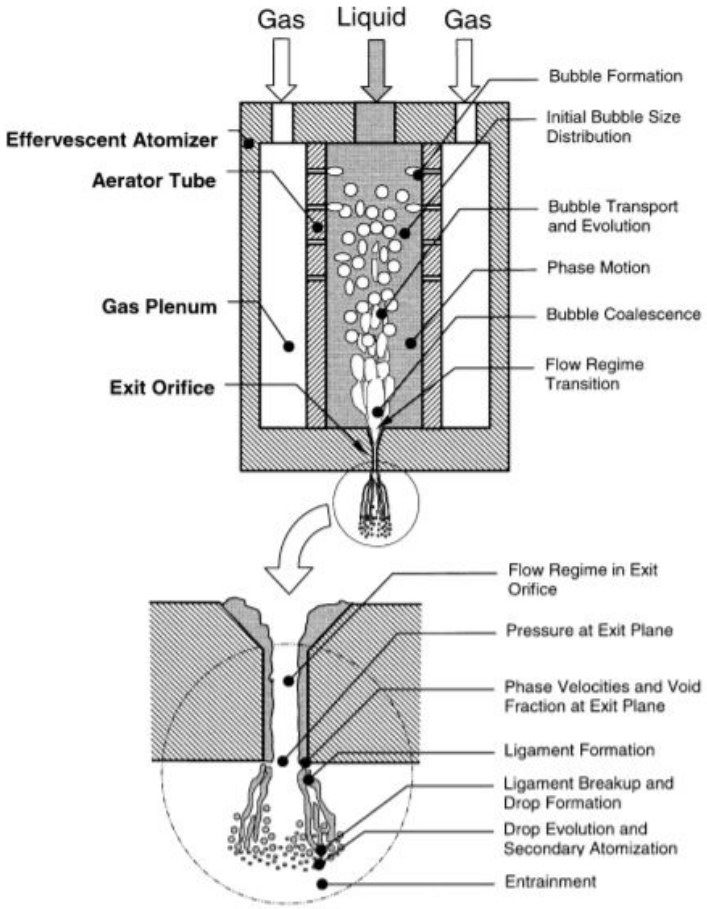

Figure 2.5: (a) Cross section of a typical effervescent atomizer (b) Gas–liquid interaction at the exit orifice [22]

almost independent of viscosity. Though on the other hand, the configuration has certain limitations that restrict it's industrial scale deployment. There's a theoretical limit upto which you could potentially inject air/gas into the liquid stream.

Whitlow & Lefebvre [36] have shown that by assuming 1-D steady state mixing chamber, the maximum GLR (Gas to Liquid Ratio) that can be achieved is given by Eqn 2.21.

$$GLR_{max} = 4.6\frac{\rho_g}{\rho_l} \tag{2.21}$$

GLR_{max} refers to the upper limit that one could achieve with effervescent atomizer ($\rho_l >> \rho_g$). The scope to achieve very fine atomization by going to higher GLR is somewhat limited. In the next section, we'll look at flow-blurring nozzle concept that has recently gained a lot of scientific attention. This nozzle was actually used in the present experimental work to establish a baseline for comparison.

Flow Blurring : Ganan-Calvo [10] reported the development of a efficient atomizer with a novel flow pattern. The nozzle construction shown in Fig 2.6(a) is similar to a co-flow nozzle explained in detail in the earlier section. The flow pattern is governed by a simple geometric ratio represented as $\psi = H/D$. When $\psi > 0.25$, the liquid flow follows the well known flow-focussing pattern as typically seen in co-axial twin-fluid atomizers. When ψ drops to a value below 0.25, the flow pattern experiences a bifurcation at the exit of the liquid tube. The gas becomes significantly radial leading to the development of a stagnation zone between the liquid tube exit and the orifice. Part of the gas stream flows into the liquid tube causing turbulent mixing within the nozzle as shown in Fig 2.6(b). Ganon-Calvo claims that the FB atomizer is about 5-50 times more droplet surface area than other pneumatic atomizer of 'plan-jet airblast type'. The backflow of atomising gas stream increases the local pressure and results in intense mixing process. As the 2-phase mixture enters the orifice, the pressure decreases and results in rapid expansion of air bubbles to breakdown surrounding liquid into fine droplets[27]. Since the 2-phase mixing occurs at the end of liquid tube, the Flow Blurring atomizer overcomes drawback of Effervescent atomization such as need for high pressure atomizing air. FB atomizer has shown superior performance with biofuel combustion [27].

Ganon Calvo presented the Eqn 2.22 has a best fit to several experimental measurements with orifice diameter ranging from 100μm to 600 μm.

$$\delta = 0.42We_D^{-0.6}(1 + 18Oh_D)(1 + \frac{1}{GLR})^{1.2} \tag{2.22}$$

This experimental correlation would then be used to validate the results obtained in the present work for flow blurring atomizer.

The flow blurring nozzle has two major challenges for adoption. First, It's difficult to exactly maintain ψ at a value below 0.25. Secondly, the flow pattern and behavior is chaotic with little room for modeling and improvement. Attempts to further improve it's performance or custom control the resulting droplet spectrum is very difficult. In

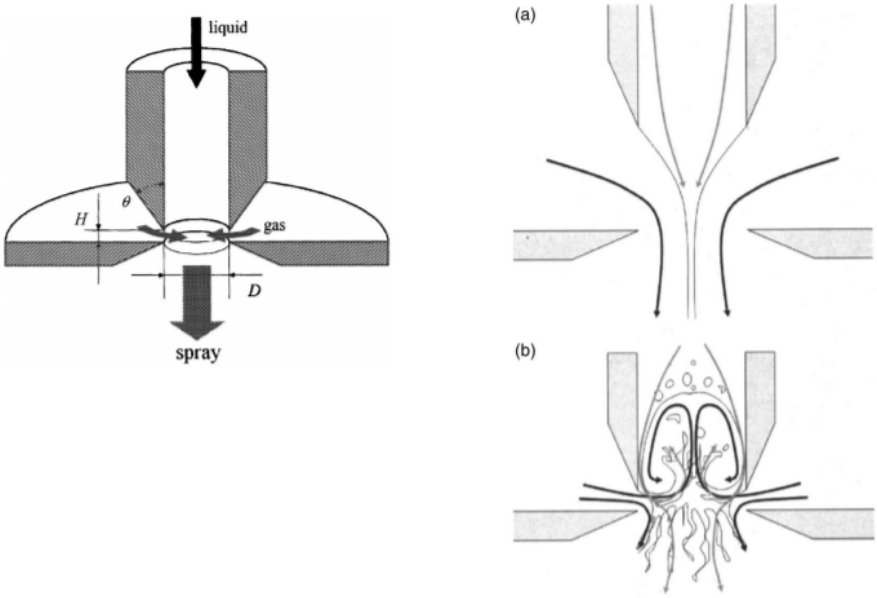

Figure 2.6: (a) Cross section of a typical flow blurring atomizer (b) Flow pattern within the nozzle (i) $\psi > 0.25$ (ii) $\psi < 0.25$ [10]

the present work, an alternative novel design is discussed based on counterflow shear theory. Before proceeding the discussion on counterflow nozzle, let's take a closer look at single phase counterflow theory.

Counterflow Shear Theory:

Most of the studies describe jet exhausted into a quiescent environment. In such cases,the velocity ratio $R = (U_1 - U_2)/(U_1 + U_2)$ describing the jet mixing region is always equal to one. The difference velocity $\Delta U = (U_1 - U_2)$ describes the shear intensity across the layer, where U_1, and U_2, are the uniform velocities on the high and low speed sides of the layer, respectively, and $U_{av} = (U_1 + U_2)/2$ is the average speed of the streams. In a generalised sense, we can consider mixing-layer velocity ratios from zero to infinity, the former corresponding to a wake, and the latter to equal and opposite streams also known as the Kelvin-Helmholtz(KH) instability[32]. When $R < 1$ a coflowing mixing region is established, as shown in Fig 2.7 (a), where the streams U_1, and U_2, travel in the same direction. When $R > 1$, a counterflow mixing region is established as shown in Fig 2.7 (b) with the two fluid streams travelling in opposite directions. The counterflow field was established by applying suction to the periphery

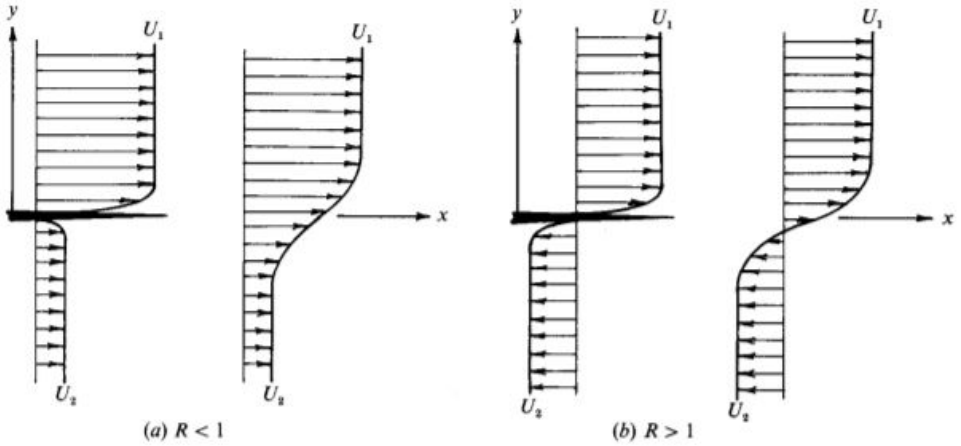

Figure 2.7: Schematic sketch for (a) Co-flow stream (b) Counterflow stream [32]

of an axisymmetric jet. Strykowski[32] finds that above a critical ratio (R_{cr}) of 1.32 , energetic oscillations in the shear layer lead to very organized axisymmetric vortex structures in the mixing layer. This experimental result for very thin axisymmetric jet compares favorably to the theoretical prediction of R_{cr} of 1.315 for transition from convective instability to absolute instability by Huerre & Monkewitz [15].

Forliti [9] shows development of thick mixing region with instantaneous bulk mass exchange between the two fluid streams. Peak turbulence quantities showed a remarkable transition to absolute instability when the counterflow velocity reaches just 13% of the primary stream velocity. This is accompanied with the presence of 3-dimensional flow & large scale vorticity that have not been clearly understood.

It's clearly established from the previous discussion that the counterflow fluid velocity helps improve turbulent mixing in case of single phase flows. Further systematic study would be required to understand the effect of wall confinement & multiphase flows in the counterflow mode. The present work utilises a nozzle based on hypothesised superior mixing of two fluids using counterflow shear interaction.

Counter nozzle : Counterflow works on a similar principle to that of a flow blurring atomiser in the sense that the air velocity is completely impinged on to the liquid surface through a thin gap as shown in Fig 2.8. The air jet entering through the annulus is made to take a reversal in direction and enter through a thin gap. The reduction in

flow area accelerates the air stream leading to the creation of intense counterflow shear layer between the liquid and air. While effects of 2-phase flow such as viscosity, surface tension & confinement in geometry haven't been explored by Strykowski [32], there is reasonable evidence to suggest a better mixing between two immiscible fluids occurs to due counterflow interaction.

This turbulent scale interaction leads to the creation of 2-phase bubbly mixture which then exits the orifice as a fine spray. It is also believed that the presence of shock waves near the nozzle exit due to drop in sonic velocity for 2-phase flows might be influencing the nozzle performance. It goes beyond the scope of the present work to investigate the internal mixing characteristics of a counterflow nozzle.

Hoxie [14] investigated the use of a novel atomizer deploying countercurrent configuration. It was primarily found to exhibit characteristics similar to all internal-mixing nozzles. Experimental results indicated much superior performance at higher liquid flow rates and lower ALR of about 0.2 suggesting a over 100% improvement over a commercial nozzle chosen in the study. The authors did not explain the physical mechanism responsible for driving the superior performance.

Strykowski's Atomization model :

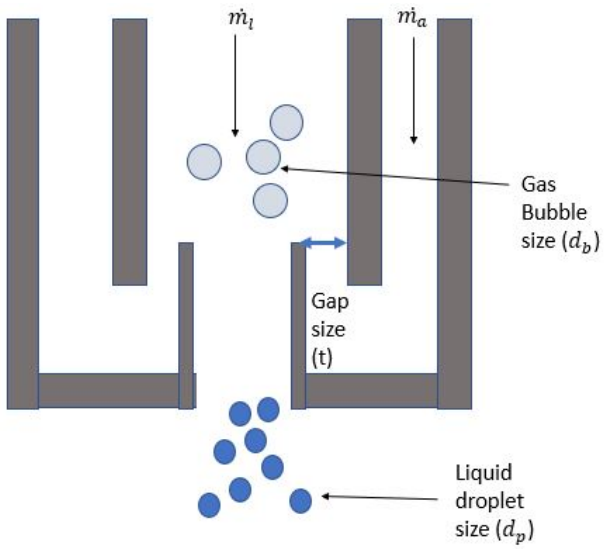

Figure 2.8: Schematic sketch for Counterflow Atomisation model [32]

Strykowski developed a atomization model based on incompressible mixing of 2 fluids

occurs at very high gas velocity. This radical mixing due to turbulent interaction in the counterflow shear layer leads to homogenous bubble size (d_b). Two key assumptions used in the model are :

- $d_b \simeq t$: Bubble size generated inside the 2-phase mixture is proportional to some characteristic length scale. In this work, it has been reasonably hypothesised to be scaled with gap size (t).
- $\dot{N_P} \simeq \dot{N_B}$: If the droplets formed in the near field by effects of a uniform gas bubble size, it's sensible to assume that the number of droplets emerging out of the orifice scales with the number of bubbles in the 2-phase mixture.

Bubble generation equation is given by Eqn 2.23.

$$\dot{N_B} \simeq \frac{Q_G}{V_B} \simeq \frac{\frac{\dot{m_G}}{\rho_G}}{t^3} \simeq \frac{\dot{m_G}}{\rho_G t^3} \tag{2.23}$$

Similarly droplet generation is given by Eqn 2.24 and size is given by 2.26

$$d_p^3 \simeq V_p \frac{Q_l}{\dot{N_P}} \simeq \frac{Q_l}{\dot{N_B}} \simeq \frac{\dot{m_L}/\rho_L}{\dot{m_G}/\rho_G t^3} \simeq \frac{\rho_G}{\rho_L} \beta^- 1 t^3 \tag{2.24}$$

$$d_p^3 \simeq \frac{\rho_G}{\rho_L} \beta^{-1} t^3 \tag{2.25}$$

$$\frac{SMD}{g} = c \frac{{\rho_G}^{1/3}}{\rho_L} \beta^{-1/3} \tag{2.26}$$

The rho_G was taken as the density of gas at ambient pressure to which the spray is released unto since it obtained a better fit on the experimental data. Eqn 2.26 would be later used to compare the experimental results and gain further insights into the mixing process within the nozzle which actuals dictates the spray quality outside the orifice exit.

Eric's (2019) earlier work on counterflow explored the effect of gas molar mass on performance of the nozzle. It was noted that the Gas molar mass has significant influence of mean droplet diameter which is in stark contrast to co-flow or effervescent atomizers. Lighter gases tend to produce sprays with smaller mean droplet diameter. The observed experimental results matched well with the non-dimensional model given by Eqn 2.26 suggesting appropriate length scale(gap size or t) used.

Measurement Technique : Measuring the droplet spectrum in sprays is challenging when compared to most aerosols due to their high mass fractions [33]. Phase doppler particle analysis (PDPA) is an interesting alternative to the shadowgraphy technique used in this work. PDPA uses a small sampling volume (in the range of 500 μm) and introduces ambiguity for dense sprays when multiple droplets cross the volume. It also limits the largest drop size captured and requires long recording to capture statistically significant number of droplets as outlined in Table 2.2 [28]. Imaging based techniques can overcome these limitations by providing a high resolution size measurements over a relatively large field-of-view from the captured images so that the recording duration is kept reasonably small [18].

One of the major drawbacks associated with imaging techniques for measurement of drop sizes is the tedious,time-consuming and often subjective analysis of photographs. It is difficult to determine diameters of droplets on a blurred image and the analyst must use some discretion in determining in-focus drops. Since the transition between an in-focus image and a blurred image is gradual, there exists a range of image quality that need to be filtered with an objective criterion[3]. This drawback could be eliminated if we choose to impose a threshold parameter to determine in-focus droplets and discard the rest of the measurements. Another key component to Image analysis, is the use of automated macro within Imagej software to ensure repeatable measurement (free from operator bias). The present work using a combination of ImageJ macro and a MATLAB correction to obtain reliable result as outlined in Chapter 4.

Chapter 3

Motivation & Goals

Based on the earlier discussion, one could arrive at the conclusion that counterflow shear promotes mixing of fluid streams in case of single phase interaction. The counterflow nozzle developed with this in mind needs to investigated further. It remains to be seen whether the superior inviscid mixing that occurs in single phase flows could be felt for 2-phase confined flows with effect of viscosity and surface tension. To explore effect of viscosity on nozzle performance, the variables of interest are determined and a test matrix is developed. The spray quality developed by a nozzle has been shown in the previous section to be dependent on air to liquid ratio, Weber number and ohnesorge number. This study looks at spray quality at various axial and radial location ensure complete spatial reconstruction.

For defining the spatial field, additional non-dimensional length scales have been defined. Radial distance (r/d0) has been been defined as the ratio of radial distance from the central axis of the nozzle to the nozzle exit diameter. Downstream distance (z/d0) has been defined as the ratio of distance from nozzle exit plane to the nozzle exit diameter. Nozzle exit diameter has been fixed at 1.55 mm for the present work.

In short, the objectives of the present study are to:

- Characterize the effect of viscosity on counter flow nozzle for a range of fluids from viscosity of 1 to 133.5 mPas.
- Measure spray quality variation across spatial domain for varying Air to Liquid Ratios.

Nozzle Type	Axial Location (z/d0)	Radial Location (r/d0)	Fluid	Air to Liquid ratio (β)
CF	10, 20, 30, 50, 70	0	Water, PG	0.5
CF	30,50	0	Water, PG, Gly85	0.25, 0.5, 0.75, 1
FB	30,50	0	Water, PG, Gly85	0.25, 0.5, 0.75, 1
CF	30,50	1,3,5,7	Water, PG, Gly85	0.5

Table 3.1: Experimental matrix for studying counter-flow nozzle

- Develop a metric to compare performance of counter flow nozzle with flow blurring nozzle.

Chapter 4

Experiment

Majority of experimental results reported in this study were conducted within a spray chamber developed in Multiphase Transport Phenomena Lab (MTPL) at University of Minnesota-Twin Cities. The tests in this study were conducted in a quiescent atmospheric spray chamber at room temperature.

Liquid	Density (kg/d^3)	Viscosity (mPa.s)	Surface tension(mN/m)	Oh
Water	998	0.9	72	0.0027
Propylene Glycol (PG)	1042	49.3	36	0.23
Glycerol-Water (85%-15% v/v)	1229	133.5	66	0.45

Table 4.1: Properties of the three fluids used in the present work

4.1 Overview of Apparatus

The experimental setup is shown schematically in figure 4.1. Pressures up to 6 bar and flow rates of up to 80 g/s can be attained. The beam from a pulsed Nd:YaG laser (Beamtech Vlite 200, 532 nm, 200 mJ/pulse, pulse-width 6 ns) operating at 15 Hz is expanded using optics and further diffused by a plastic sheet which serves as a backlight against which droplets are illuminated. Images of size 24 megapixels are acquired using a Canon EOS 77D camera coupled to a K2 Distamax long working-distance microscope

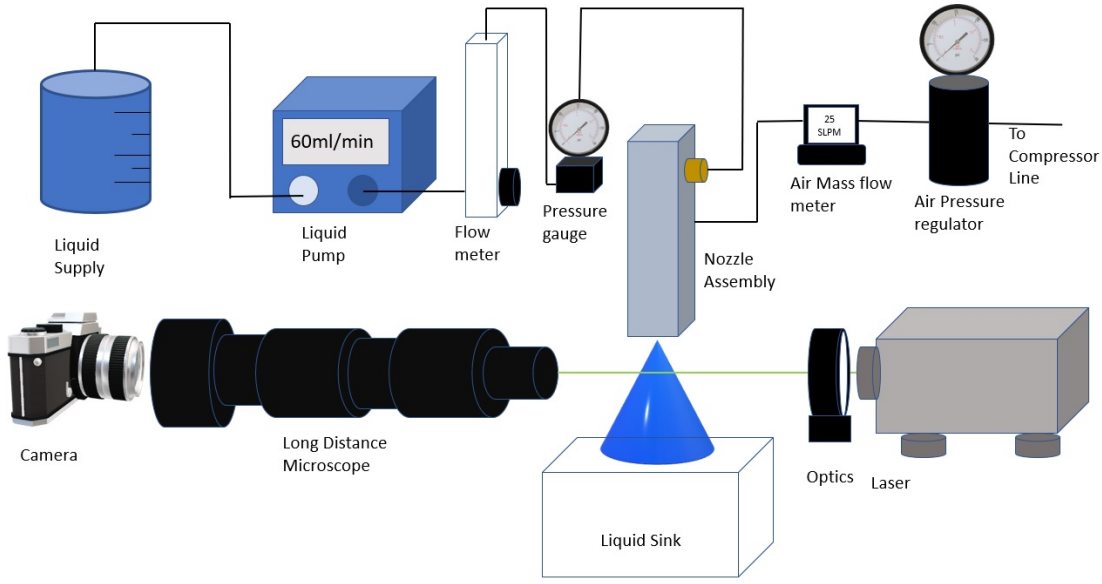

Figure 4.1: Counter-flow Experimental Setup

with a CF4 objective lens. This produces an image with a magnification of 0.55 microns/pixel, and a field of view of approximately 3.3 x 2.2 mm. Image processing is performed using the software ImageJ.

The majority of droplets were sufficiently small that depth-of- field corrections were not considered necessary. Droplet statistics were extracted by ensemble averaging over 1000 images, which typically yielded in excess of 20,000 droplets in all cases considered. Droplets below a diameter of 3.5 microns (7 px by 7 px) were ignored when calculating statistics. For this data reduction procedure, the calculated droplet diameter changed by less than 1 micron when half the images were considered, and this value is taken as a measure of uncertainty. Flow visualization was conducted using a Photron Mini AX200 high speed camera operating at 3000 frames/second.

4.1.1 Nozzle Assembly

The nozzle assembly primarily consists of outer hollow tube, inner liquid tube and nozzle end-cap. This modular approach is designed so as to permit availability to switch between different nozzle configurations. A complete description of nozzle combinations

has been described in the appendix. For the present study, we have focused on 2 specific nozzle configuration; D2 (Counter-flow) & A9 (Flow-Blurring) nozzle as shown in Figure 4.2.

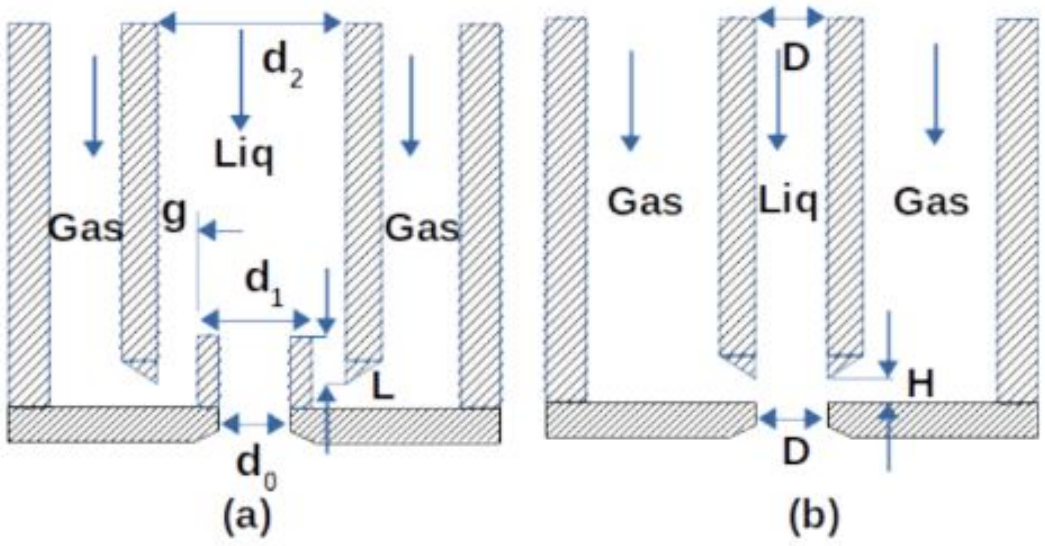

Figure 4.2: (a) D2- Counter-flow Nozzle (b) A9- Flow-Blurring Nozzle

For the counterflow nozzle, d0=1.55 mm, d1=1.7 mm, d2=2.1 mm was used in the D2 configuration. For the flow blurring nozzle, D=1.55 mm and H=0.3 mm was used in the A9 configuration. In both sets of nozzle, 4 sets of M8 nut & bolts were used to rigidly clamp the endcap to the outer tube of the nozzle assembly. The entire nozzle assembly has been built on a manual multi-axis Thor labs micrometer stage. This permits precise control over nozzle exit location with respect to the optical rail system containing the long distance microscope. The maximum axial height that could be attained is 12 cm (80 d) from the center of the microscope.The nozzle assembly is tightly clamped to the vertical stand to ensure no movement during the course of the experiment. The entire assembly is made out stainless steel and close tolerances are maintained to ensure symmetry in flow distribution.

4.1.2 Reservoir & Flow System

The building air supply system operating at 6 bar is connected to the nozzle through a pressure regulator and air mass flow meter. Omega air mass flow meter (Model No.FMA1841A) can measure flow rates in the range of 0.8 to 80 SLPM. The air pressure regulator helps in controlling the actual air to liquid flow rate that occurs within the nozzle. It houses an in-built filter to avoid accumulation of debris within the nozzle. We have attempted to pump higher air flow rates at higher pressures by coupling this system to a pressurized cylinder. However, most reported results in this work do not use air supply from a cylinder. On the other hand, a constant supply of liquid is maintained through a 1.2-Litre graduated cylinder connected to the nozzle through a gear pump. Care is taken to ensure that the liquid reservoir is completely covered and at room temperature. A flexible plastic tubing is used for the entire fluid circuit. A Cole Parmer gear pump (Model No. 75211-70 "V21" size) was used for overcoming the pressure losses. It can handle flow rates upto 151 mL / min. For the present study, we have restricted ourselves to a constant liquid flow rate of 60 mL/min for all the 3 liquids (Water, Propylene Glycol and Glycerol 85% soln) to ensure consistent results. We have added a rotameter to the exit of the gear pump to validate the expected liquid flow rate. A liquid pressure gauge is connected in the liquid line right before it enters the nozzle.The entire system is made leak proof by appropriate use of fluid couplings.

4.1.3 High speed flow visualisation

For the purposes of obtaining near nozzle exit features of the spray, High speed imaging has been used. Photron Mini AX200 has a maximum frame rate of 216,000fps and an independent controllable electronic shutter up-to 260 ns. It's connected to the Computer using a ethernet cable to ensure quick transmission of information. It has produces a continous stream of images (1024px by 1024px) which could then be replayed at slower speeds to extract vital information. A high power continuous LED light source along with a teflon diffuser is used to provide a uniform bright background for the spray imaging. Canon extension lens is used to focus on object of interest and ensure near field characteristics are accurately captured. For efficient data storage, all videos have been cropped to less than 10Gb (10,000 images) per data point.

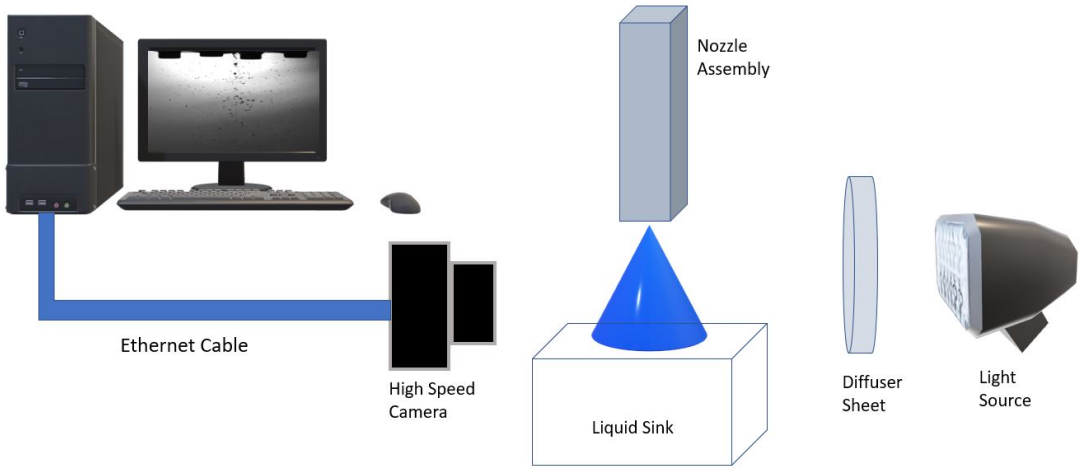

Figure 4.3: (a) High Speed Imaging

4.1.4 Shadow graph Imaging System

Beamtech Vlite 200 green laser was used as the light source for shadowgraph imaging. It emits a 6-8 ns pulse of 532nm with an adjustable repetition rate of 1-15Hz. This causes the droplets to essentially freeze in space due to shutter exposure times of the order of several milliseconds. The laser has 99.8% spectral purity with jitter times of less than 0.5 ns.The laser is aligned behind the Thor labs expanding optics using the optical table. A Canon EOS 77D camera is coupled to K2 Distamax long distance microscope with interchangable objective lens. For baseline study at an axial distance of 30d, CF-4 objective lens with a magnification of 0.717μm/px and a field of view (FOV) of 4.2mm*2.8mm. For all other axial downstream distances (10d,20d,50d,70d), CF-2 objective lens with a magnification of 1.91 μm/px and a FOV of 11.5mm*7.6mm. The entire microscope assembly is placed on the optical table using a Thor labs rail to maintain alignment the laser. The entire assembly is covered with black sheet to ensure minimum interference from ambient light.

4.2 Procedure

4.2.1 Safety Precautions

The following precautions were taken to ensure safe practices during the course of the experiments.

1. Wear Safety Goggles of appropriate wavelength at all times during the course of the experiment.
2. Clean and wash hands before and after usage of chemicals.
3. All chemicals must be in clearly labelled containers.
4. Make sure the Laser is turned off whenever not in use.

4.2.2 Pre-Lab Preparation

1. Note that the right nozzle configuration has been mounted on the assembly.
2. Using a graduated cylinder, calibrate the gear pump liquid delivery for given liquid at a specific air flow rate.
3. Perform sanity checks to ensure there is no leakage of air or fluid.
4. Ensure enough (at least 500ml) solution of desired liquid to be utilised.
   (a) Prepare solution using Hot plate and measure accurate quantities of solution mixture.
   (b) Insert magnetic stirrer and tightly seal the solution bottle with plastic cover to avoid external contact.
   (c) Let the solution stir for at least 3 hours (using timer in the lab) on the hot plate and for 24 hours off-plate before usage.Ensure optical consistency in the completely mixed solution.
5. Ensure that the microscope is focused on the central plane along the axis of the nozzle.

(a) Lower the nozzle assembly to the align with the microscope. Fine control could be used to center the image using the micrometer stage.

(b) Invert the endcap to have the hypodermic needle pointing outward.

(c) Adjust the distance between the objective lens and the hypodermic needle to obtain clear focus on the central plane.

4.2.3 Microscopic Imaging

1. Clean the objective lens with IPA solution and DI water to ensure clarity of images obtained.
2. Start flow of air for about 3-5 minutes before starting the liquid pump.
3. Start the Liquid pump in continuous flow mode with desired level of flow rate per minute.
4. Increase airflow to obtain desired ALR for the given experiment.
5. Record Liquid flow rate, Air flow rate and Pressure gauge readings in the lab notebook along with the date of the experiment.
6. Operate the Camera in continuous shooting mode using trigger with the right ISO and shutter settings for the given liquid. Start the camera after about 10 seconds since the start of liquid spray.
7. Stop intermittently(if required) for cleaning the objective lens and transfer the images from the SD card to appropriate folder on the hard drive.
8. Take at-least 500 images for a single data set before proceeding to taking the next data set.

4.2.4 High Speed Imaging

1. Remove the end cap and rinse it clean before starting the experiment.
2. Start flow of air for about 3-5 minutes before starting the liquid pump.

3. Connect the High speed camera cable to the Computer by changing IP settings to 192.168.0.XXX where XXX can be any 3 digit Number like 123.

4. Open PFV Application and check the for optimum lighting conditions (Frame rate & Shutter speed)

5. Start the Liquid pump in continuous flow mode with desired level of flow rate per minute.

6. Increase airflow to obtain desired ALR for the given experiment.

7. Record Liquid flow rate, Air flow rate and Pressure gauge readings in the lab notebook along with the date of the experiment.

8. Once set, quickly hit Record & TriggerIn to start capturing. Stop once you have hit the desired length of image/video capturing. Save File name as LiquidVolFraction_Configuration_LiqFlowrate_Airflow After completing trials, transfer image/video folder to Google drive or ENET shared drive Rhome/m-mtp/ranga055 folder and upload to google drive. E.g Glycerol85Water15_D2_37.5(SLPM)

9. Stop the gear pump (liquid line) first and then reduce air flow rate using the pressure regulator after completion.

4.2.5 Troubleshooting

Pump Issues :

Depending upon the source of the issue, the solution would vary. If the liquid reservoir gets too low during the course of the experiment, the gear pump would start to draw in air and develop air pockets in the liquid line. To avoid this, it's best to ensure that the suction line is firmly immersed in a solution of at least 500ml at all times before starting the experiment.

There could be a difference in expected fluid delivery to actual fluid delivered to the nozzle. If this occurs, try to re-calibrate the pump for the given fluid and restart the entire experiment. To avoid this issue, ensure that calibration is always the first step before starting any experiment with this gear pump.

Pump suddenly stops working even though the liquid reservoir was adequately filled.

This happens due to overheating of the gear pump under long hours of operation. Switch off the pump and restart the pump after a 30 minute cooling period to check for issues. To avoid this issue, ensure that the pump is switched off and not merely paused for operation whenever it's not in use.

Camera Issues :

It's possible that under the continuous shooting mode, the camera throws an exception error. This is most likely due to either higher shutter speeds or low battery conditions. Replace a charged battery and restart the camera to overcome this issue.

Even under continuous shooting mode, if you obtain only single shot images then check if external trigger option is turned on.It's good practice to often disconnect the camera from the microscope and shoot a couple of pictures around in the lab to ensure that the trigger performs as expected.

The images captured are not read into the SD card. Try to format the SD Card and insert it again slowly into the slot.Always ensure that the camera is switched off when you are trying to switch SD cards.

Microscope Issues :

It's possible that the spray hits the microscope body or lens during the course of the experiment. We have little control over this since the spray angle dictates this behavior and the proximity is decided by the focal length of the microscope. Try to use a air curtain or a funnel to avoid droplets hitting the objective lens. For higher axial distances, use a larger focal length objective lens such as CF-2.

If you obtain interference patterns on the images captured. Try to clean the entire optical setup with IPA and DI water solution. Leave it alone for sometime before using a clean lens cloth to remove any dirt or dust on the surface. To avoid this issue, keep all the optics covered whenever they are not in use. These patterns may also be obtained if there is a misalignment in the camera position with respect to the laser. Correct alignment is a prerequisite to obtaining good images with clean background.

Flow meter issues :

Air mass flow meter reads a fluctuating value within 0.1 SLPM during the course of the experiment. This is due to minor pressure fluctuations occuring within the nozzle. If this mass flow meter stops reading accurately, it's most likely due to presence of liquid in the air tubing. This occurs when the air flow is stopped before the liquid line is

stopped. To overcome this, open the air tubing before and after the flow meter and leave it to dry for 1-2 hours after blowing compressed air over it.

Chapter 5

Analysis

5.1 Analysis Procedure

Data Acquisition : All images for a particular dataset are saved within the same folder. A common nomenclature for naming of the folders was followed for the purpose of consistency. Liq_NozzleType_Location_ALR is used with common abbreviations to denote Liquid type (Gly85 : Glycerol 85% ,PG : Propylene Glycol)& Nozzle Type (CF : Counterflow nozzle , FB : Flow Blurring).

ImageJ Processing : Imagej software developed by National Institute of Health (NIH) was used for extracting the droplet information from the images. A customised macro was developed to summarise this information in a tabular form. This information is then saved as a excel sheet. A single raw image and a corresponding processed image obtained using Imagej is shown in Fig. 5.1.

MATLAB : The excel sheet saved in the earlier step is then imported in matlab code and useful parameters such as sauter mean diameter, Cumulative volume distribution parameters (d10,d50,d90) is calculated within this code.

5.1.1 Data Processing

MATLAB code was written to extract useful parameters such as Sauter Mean Diameter (SMD) and efficiency (η). There is an image correction filter applied in the code which accounts for scenarios in which blank images are encountered. MATLAB is also used to generate plots for parameters of interest in this study. MATLAB code requires 3 inputs

for processing the code :

- **Magnification Factor** : Imagej processes the raw data as a single 2D pixel matrix. In order to make physical sense of the result, it is necessary to convert the pixel data into standard units such as microns using Magnification factor. An image is captured with the inverted endcap with the needle pointing outside. With a known outer diameter of the needle, an image is captured to measure the pixel diameter of the needle. We take the average value of 3 such diameter measurements to ensure that we obtain an appropriate magnification factor. Note that the magnification factor depends upon the objective (CF-2 or CF-4) used in the experiment.

- **Results** : The output of the Imagej macro can be exported in a Comma separate value (.csv) Excel file. This file contains the a list of droplets identified along with their areas in pixel square units. Magnification factor could then be used to determine the exact diameter of each droplet.

- **Summary** : Imagej could also export Image specific information such as % Area covered by droplets, average droplet size per Image & Number of droplets captured in the image using the macro. This information is then used to filter out blank images with unreasonably large value of droplet count.

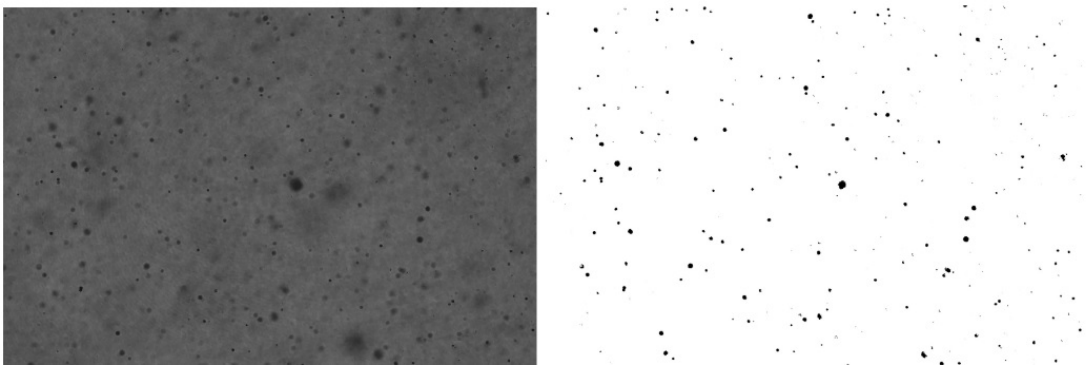

Figure 5.1: (a) Raw Image (b) Processed Image

5.2 Analysis Result

5.2.1 Qualitative Comparison

The present section shows a qualitative comparison of nozzle performance under varying conditions. All images were captured using a Canon DSLR at 1/15 shutter speed with the ISO at 400. Laser light was passed through a telfon diffuser to ensure a uniform bright background. These images were later processed using Imagej to obtain cropped image with enhanced contrast. Fig 5.2 shows the performance of CF and FB nozzle for water at 60ml/min at 0.25 ALR. Water emerges out of the counterflow nozzle as a fine spray whereas in the case of flow blurring nozzle, large droplets could still be clearly observed.

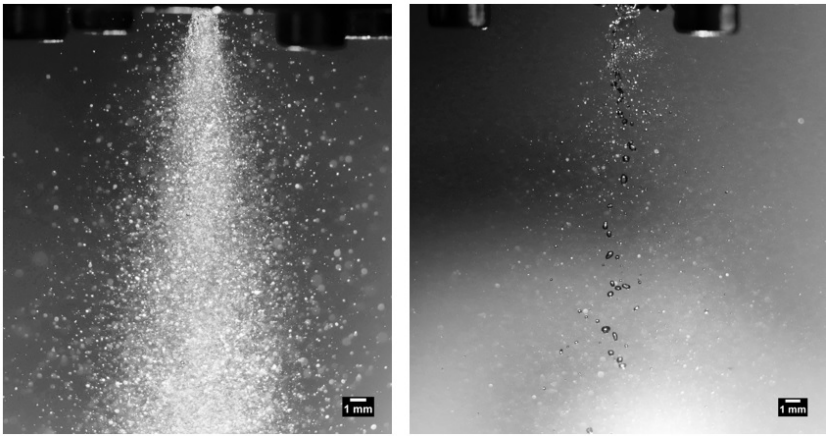

Figure 5.2: Water at $\beta = 0.25$ using (a) CF Nozzle (b) FB Nozzle

Fig 5.3 shows the performance of CF for water at 60ml/min at 4 different ALRs (0.25, 0.5, 0.75, 1). The excess air at higher ALRs doesn't show significant improvement in spray quality by means of secondary atomisation. Fig 5.4 shows the performance of CF for 3 different fluids (Water, PG and Gly85) at 60ml/min at 0.75ALR. We notice the performance to very similar in all the three cases with minor difference in the occasional appearance of larger droplets for higher viscosity fluid (Gly85).

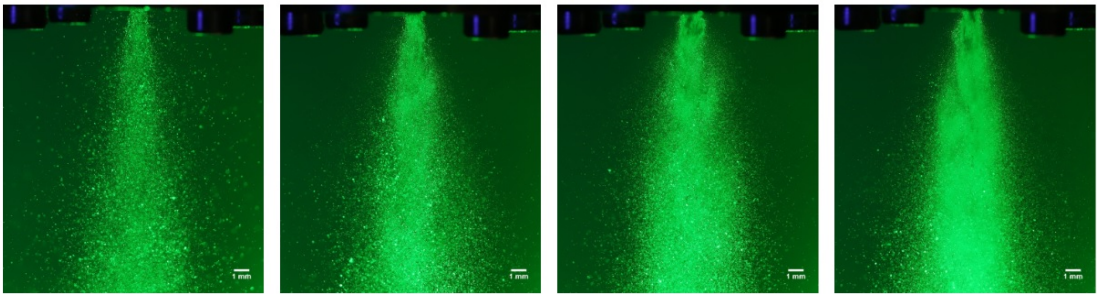

Figure 5.3: Counterflow nozzle spraying water at (a)$\beta = 0.25$ (b)$\beta = 0.5$ (c)$\beta = 0.75$ (d) $\beta = 1.0$

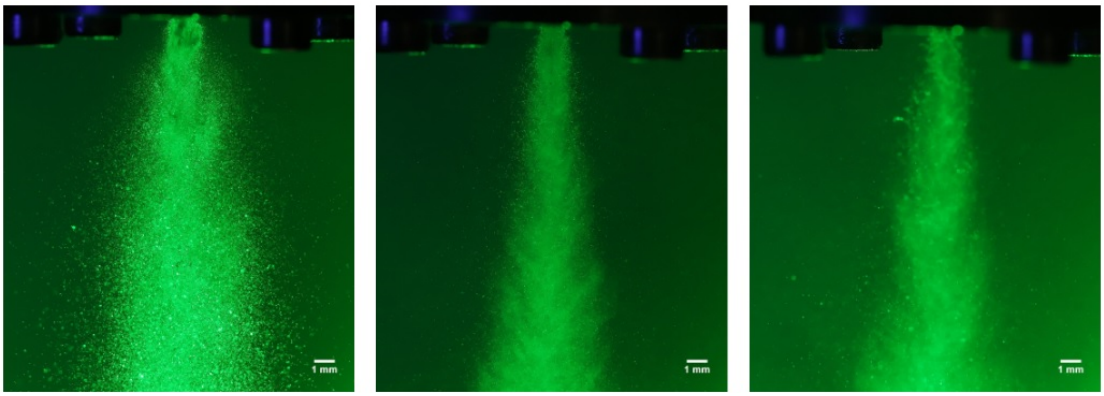

Figure 5.4: Counterflow nozzle spraying at $\beta = 0.75$ (a)Water (b)PG (c) Gly85

5.2.2 Quantitative Comparison

Fig 5.5 and Fig 5.6 show the effect of air flow rate on the liquid and air inlet pressure. We observe an expected linear trend between the air mass flow rate and air inlet pressure for 3 liquids. Fig 5.5 highlights the fact that the higher viscos fluids need to be injected at a higher pressure relative to air inlet pressure so as to overcome the pressure drop in the line.

Fig 5.7 & Fig 5.8 show the frequency distribution and cumulative volume distribution for PG at $\beta = 0.75$ using counter flow nozzle. Fig 5.7 shows a typical linearly dropping behavior on a semi-log plot for frequency against droplet diameters.

5.9 shows the comparative performance of counterflow nozzle against air blast atomiser for varying air to liquid ratio from 0.25 to 1. At $\beta = 0.25$, the air blast atomiser

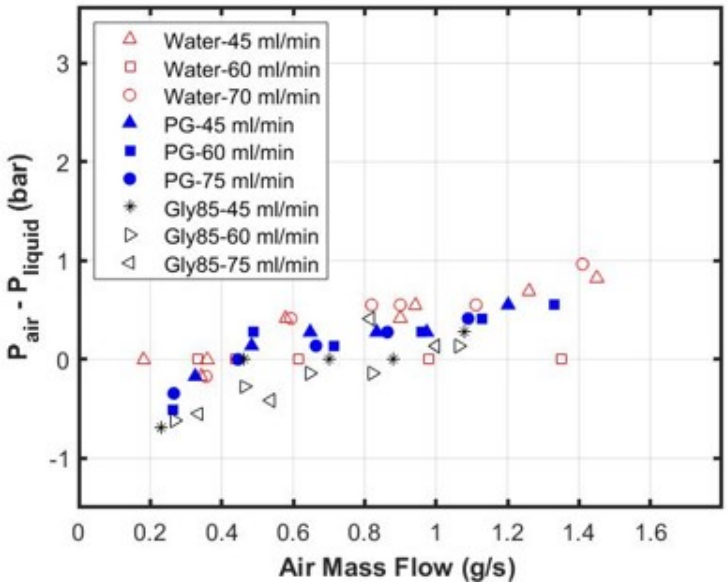

Figure 5.5: Air pressure variation with increasing air flow rate

produces droplets that are 3-5 times larger than counterflow nozzle operating under the same set of conditions. This remarked improvement in performance is possibly attributed to the better mixing between the two fluids as shown by counter flow shear theory in the background section. In 5.10, the flow blurring nozzle performance is shown along with Ganan-Calvo's model. The experimental results obtained in the present work closely match the predictions for mass median diameter (MMD) from the model. We notice that the flow blurring nozzle produces water spray mean diameters that are 5 times larger as compared to counterflow nozzle at $\beta = 0.25$.

We begin to systematically study the characterisation of the counterflow nozzle for a range of operating conditions. In fig 5.11, we observe the effect of viscosity and ALR on the spray mean diameter produced by both nozzles. Counterflow nozzle's performance is almost independent of viscosity for the range of conditions studied here. On the other hand, flow blurring nozzle produces PG spray mean diameter that are almost twice as that of water at $\beta = 0.25$. The fundamental mechanism responsible for good atomisation in counterflow nozzle is based on turbulent shear stress at the liquid -air interface leading to a performance that's less influenced by effect of viscosity. 30d :-

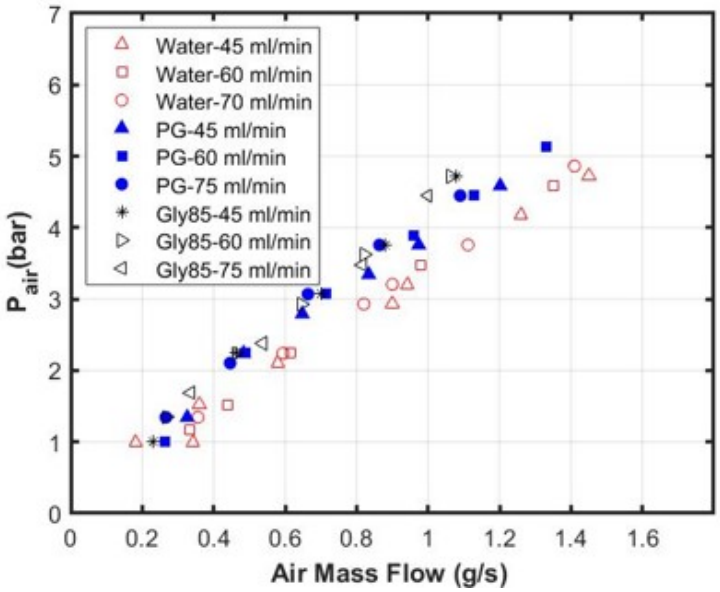

Figure 5.6: Air pressure variation with increasing air flow rate

Refers to 30 nozzle diameters (30*1.55 = 46.5mm) down from the exit plane of the nozzle. Other common acronyms are referenced throughout the document such as FB- Flow Blurring, CF- Counterflow Nozzle, PG- Propylene Glycol and Gly85- 85% Glycerol + 15% Water (v/v) soln. Next, the effect of downstream distance on spray quality produced by counterflow nozzle is shown in Fig 5.12. It's worth noting that the 30d data point was acquired using CF-4 objective and the other data points at 10,20,50 and 70d was acquired using CF-2 Objective. We observe that there is a drop in SMD value until 30d and remains constant as we move further downstream. All reported values were taken at $\beta = 0.5$ with a constant liquid flow rate at 60ml/min.

Fig 5.13 complements the earlier figure to give a complete spatial picture of spray quality. SMD values at 2 different axial locations (30d & 50d) at 5 different radial locations namely; 1d,3d,5d,7d has been shown in the figure for both water and propylene glycol. The diameters show an increasing trend along the radial direction. The larger droplets towards the periphery of the spray is expected in the case of full cone nozzle such as the one under discussion. This occurs due to the central liquid droplets being surrounded by high velocity air on all sides causing a certain degree of secondary

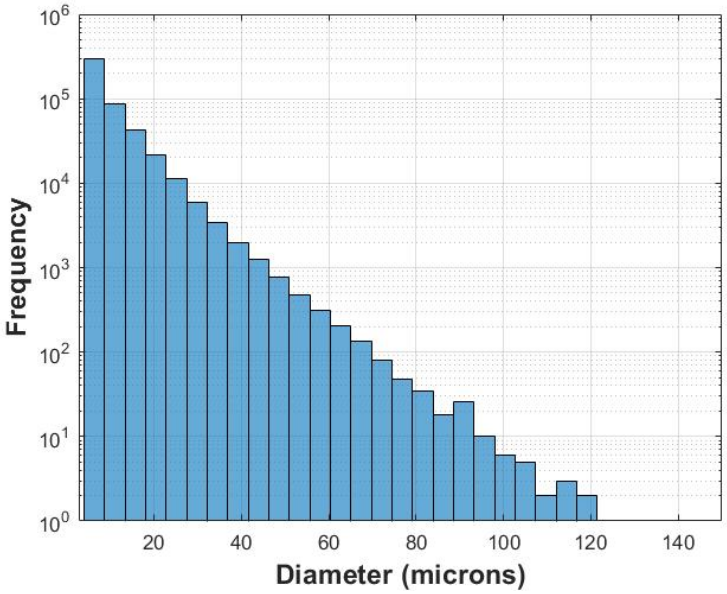

Figure 5.7: Log Scale Freq Distribution

atomisation. As noted earlier, apart from Sauter Mean Diameter (SMD), the efficiency of nozzle performance (η) forms an important metric for comparison. It accounts for the input pressure energy supplied to the air & liquid and weighs it against the output measured as work done against surface tension to produce smaller diameters. It can be seen from Fig 5.14 that for the same SMD value, the efficiency reported for a Counterflow nozzle is much higher than the flow blurring nozzle. CF Nozzle for water sprays at $\beta = 0.25$ has the highest efficiency of about 0.02%.

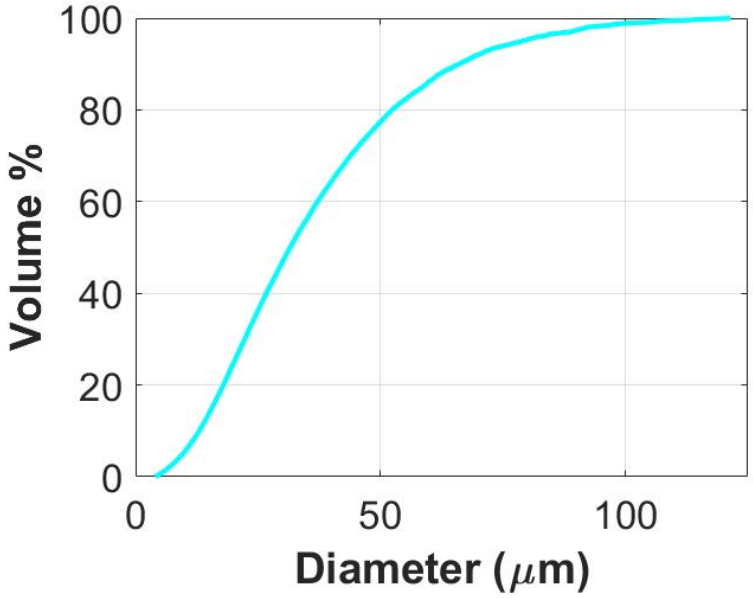

Figure 5.8: Cumulative Volume Distribution

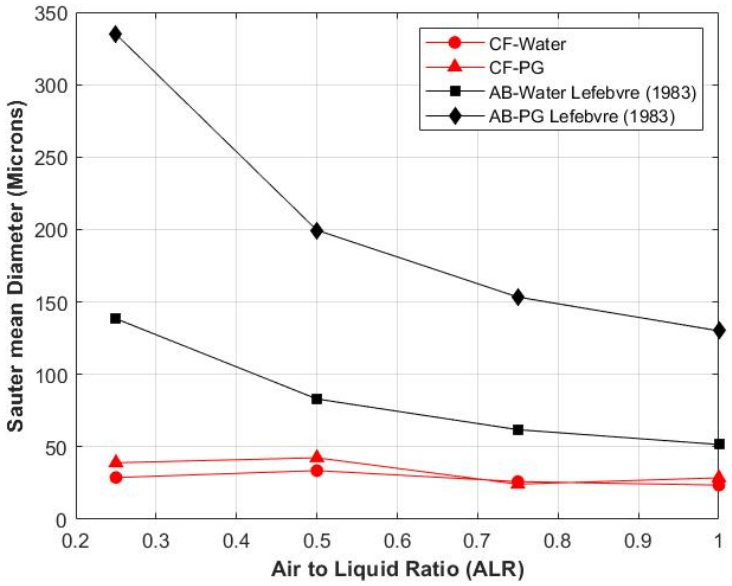

Figure 5.9: Comparison of counterflow nozzle performance with Air blast atomiser

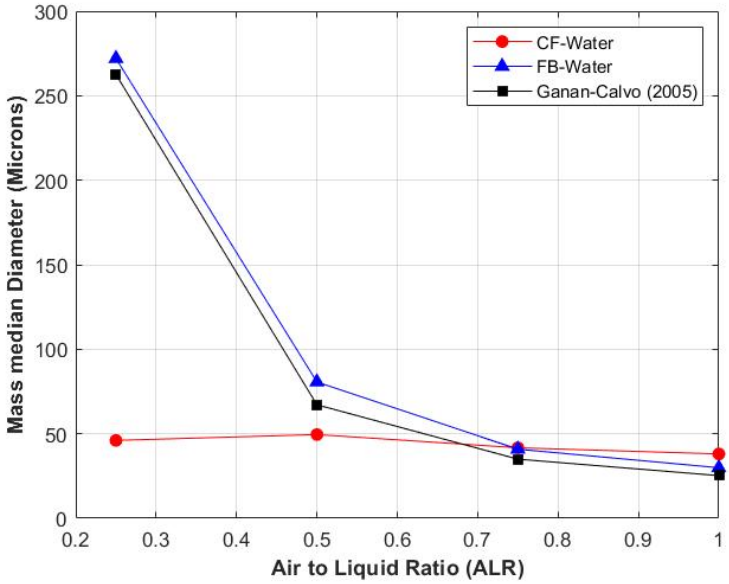

Figure 5.10: Comparison of counter flow(CF) nozzle performance with Flow blurring(FB) atomiser

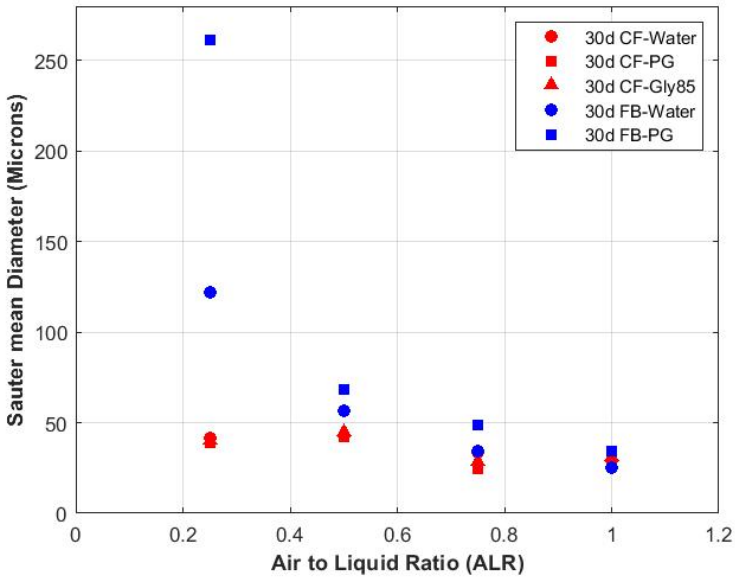

Figure 5.11: Sauter mean diameter variation with ALR

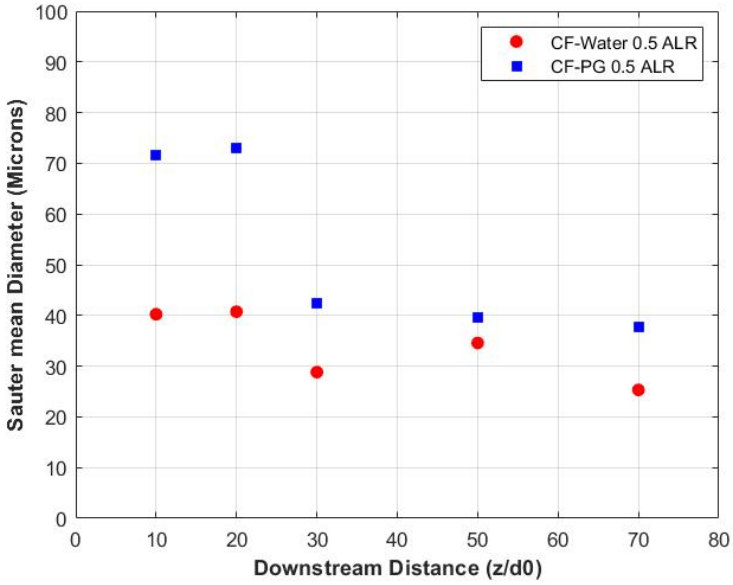

Figure 5.12: Sauter mean diameter variation with Downstream distance

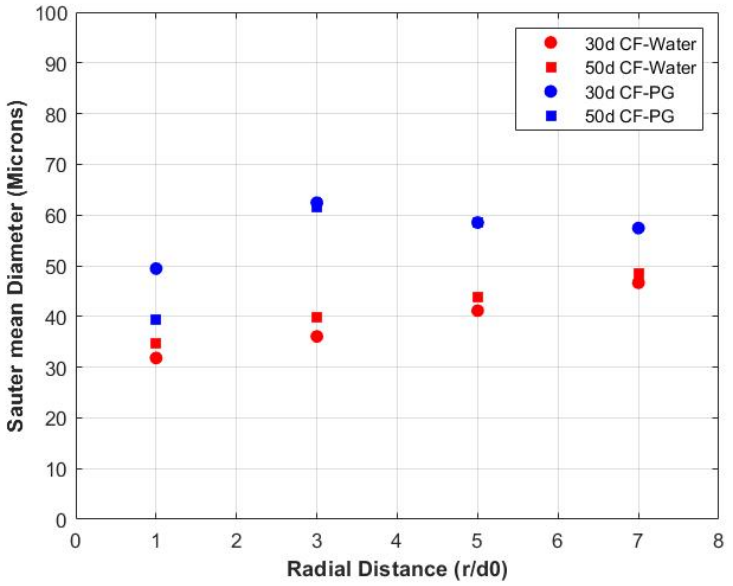

Figure 5.13: Sauter mean diameter variation with Radial distance

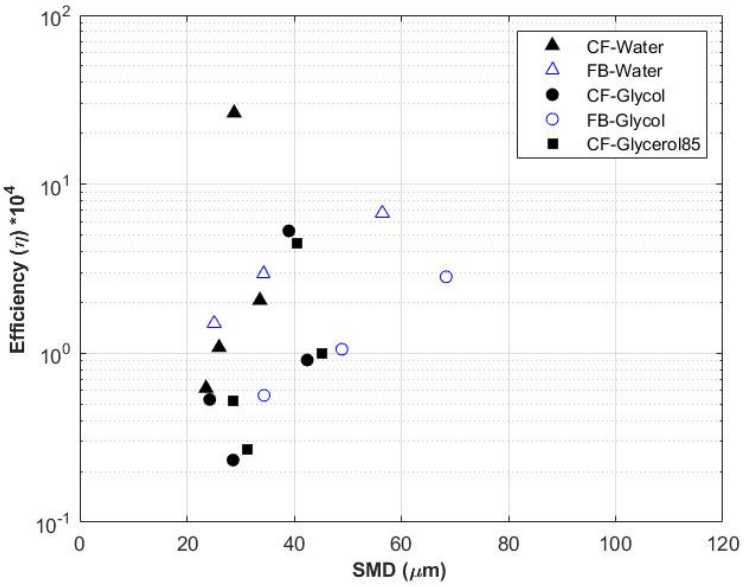

Figure 5.14: Metric to compare nozzle performance

Chapter 6

Conclusion and Discussion

The experimental facility was used to understand the effect of viscosity on the performance of counterflow nozzle. Measurements taken using shadowgraph technique have been documented. The key takeaways from this study are the following:

- Experimental data acquired for flow blurring nozzle is in excellent agreement with Ganon-Calvo's previously reported work. This serves as a good baseline for establishing the accuracy of our experimental technique.
- Both qualitative and quantitative results have shown that the performance of counterflow nozzle is superior to that of flow blurring nozzle especially at lower Air to Liquid ratio (0.25). The improvement in performance is supposedly attributed to counterflow shear theory.
- Counterflow nozzle performance is almost independent of viscosity for the range studied in this work. This behavior is not noticed with other twin fluid pneumatic nozzles such as air blast atomiser or the flow blurring nozzle. This serves as another key indicator to suggest that the fundamental mechanism driving the performance is counterflow shear. It was known that counterflow shear helps trigger a high degree of turbulent shear stress at the interface as opposed to the mean shear stress. This eliminates the significance of viscosity of the bulk fluid as much of the interaction occurs at the interface.
- The spatial variation of spray quality has also been reported in this work. The

SMD values are a strong function of the radial location and show an increasing trend as we move away from the central axis. This is alignment with expected behavior for full cone nozzles. On the other hand, SMD values change very little beyond 30d downstream from the exit plane of the nozzle. This shows that the spray exits the counterflow nozzle as a mist of fine droplet with a little scope for further reduction based on secondary atomisation.

- We observe that the spray is pulsating at a frequency of about 60Hz based on the high speed imaging data. Sprays are known for the spatio-temporal transient nature and the precise factors that affect the pulsation should be further investigated.

Further work should be carried out to understand the velocity distribution within the sprays. It's important to correlate the diameter-velocity distribution in order to understand the spray behavior. The scope of the current work has been limited to the study of newtonian fluids and an extended study encompassing non-newtonian fluids would find more interesting industrial applications. On another front, nozzles could be studied for spray cooling or spray drying applications to better extract the desired characteristics. From a physics standpoint, any point to further study the confined counterflow interaction within the nozzle would help in improving future atomiser designs. This could be achieved by developing a test rig with a transparent nozzle using air & dyed-fluid mixture.

References

[1] A. Aliseda, E. J. Hopfinger, J. C. Lasheras, D. Kremer, A. Berchielli, and E. Connolly. Atomization of viscous and non-newtonian liquids by a coaxial, high-speed gas jet. experiments and droplet size modeling. *International Journal of Multiphase Flow*, 34(2):161–175, 2008.

[2] B. Azzopardi. Measurement of drop sizes. *International Journal of Heat and Mass Transfer*, 22(9):1245–1279, 1979.

[3] L. Bayvel. *Liquid atomization*, volume 1040. CRC Press, 1993.

[4] S. Chandrasekhar. The capillary instability of a liquid jet. *Hydrodynamic and Hydromagnetic stability*, pages 537–42, 1961.

[5] N. Chigier and Z. Farago. Morphological classification of disintegration of round liquid jets in a coaxial air stream. *Atomization and Sprays*, 2(2), 1992.

[6] H. Eroglu and N. Chigier. Liquid jet instability in coaxial air flow. In *Proceedings of ICLASS*, volume 91, pages 703–710, 1991.

[7] H. Eroglu and N. Chigier. Wave characteristics of liquid jets from airblast coaxial atomizers. *Atomization and Sprays*, 1(4), 1991.

[8] Z. Farago and N. Chigier. Parametric experiments on coaxial airblast jet atomization. In *Turbo Expo: Power for Land, Sea, and Air*, volume 79061, page V003T06A016. American Society of Mechanical Engineers, 1990.

[9] D. J. Forliti, B. A. Tang, and P. J. Strykowski. An experimental investigation of planar countercurrent turbulent shear layers. *Journal of Fluid Mechanics*, 530:241, 2005.

[10] A. M. Gañán-Calvo. Enhanced liquid atomization: From flow-focusing to flow-blurring. *Applied Physics Letters*, 86(21):214101, 2005.

[11] E. Giffen and A. Muraszew. *The atomization of liquid fuels*. Chapman & Hall, 1953.

[12] D. Guildenbecher, C. López-Rivera, and P. Sojka. Secondary atomization. *Experiments in Fluids*, 46(3):371, 2009.

[13] A. Haenlein. Disintegration of a liquid jet. 1932.

[14] A. Hoxie, E. Johnson, V. Srinivasan, and P. Strykowski. Characterization of a novel energy-efficient atomizer employing countercurrent shear. In *14th Triennial International Conference on Liquid Atomization and Spray Systems, Chicago, IL, USA*, pages 1–9, 2018.

[15] P. Huerre and P. A. Monkewitz. Absolute and convective instabilities in free shear layers. *Journal of Fluid Mechanics*, 159:151–168, 1985.

[16] D. Joseph, G. Beavers, and T. Funada. Rayleigh-taylor instability of viscoelastic drops at high weber numbers. *Journal of Fluid Mechanics*, 453:109–132, 2002.

[17] D. Konstantinov, R. Marsh, P. J. Bowen, and A. Crayford. Effervescent atomization for industrial energy- technology review. *Atomization and Sprays*, 20(6), 2010.

[18] S. S. Kumar, C. Li, C. E. Christen, C. J. Hogan Jr, S. A. Fredericks, and J. Hong. Automated droplet size distribution measurements using digital inline holography. *Journal of Aerosol Science*, 137:105442, 2019.

[19] A. H. Lefebvre. Twin-fluid atomization: Factors influencing mean drop size. *Atomization and sprays*, 2(2), 1992.

[20] A. H. Lefebvre and V. G. McDonell. *Atomization and sprays*. CRC press, 2017.

[21] S. Lin and R. Reitz. Drop and spray formation from a liquid jet. *Annual review of fluid mechanics*, 30(1):85–105, 1998.

[22] M. Lund, P. E. Sojka, A. H. Lefebvre, and P. Gosselin. Effervescent atomization at low mass flow rates. part i: The influence of surface tension. *Atomization and Sprays*, 3(1), 1993.

[23] A. Mansour and N. Chigier. Air-blast atomization of non-newtonian liquids. *Journal of Non-Newtonian Fluid Mechanics*, 58(2-3):161–194, 1995.

[24] L. Rayleigh. On the capillary phenomena of jets. *Proc. R. Soc. London*, 29(196-199):71–97, 1879.

[25] L. Rayleigh. Xvi. on the instability of a cylinder of viscous liquid under capillary force. *The London, Edinburgh, and Dublin Philosophical Magazine and Journal of Science*, 34(207):145–154, 1892.

[26] N. Rizk and A. Lefebvre. Spray characteristics of plain-jet airblast atomizers. 1984.

[27] B. M. Simmons and A. Agrawal. Spray characteristics of a flow-blurring atomizer. *Atomization and Sprays*, 20(9), 2010.

[28] S. Soid and Z. Zainal. Spray and combustion characterization for internal combustion engines using optical measuring techniques–a review. *Energy*, 36(2):724–741, 2011.

[29] S. Sovani, P. Sojka, and A. Lefebvre. Effervescent atomization. *Progress in energy and combustion science*, 27(4):483–521, 2001.

[30] J. Strutt and L. Rayleigh. On the instability of cylindrical fluid surfaces. *Phil. mag*, 34(5):177–180, 1892.

[31] J. W. Strutt and L. Rayleigh. On the instability of jets. *Proc. London Math. Soc*, 10(4), 1878.

[32] P. J. Strykowski, D. Niccum, et al. The stability of countercurrent mixing layers in circular jets. *Journal of Fluid Mechanics*, 227:309–343, 1991.

[33] M. Tang, S.-C. Chen, and D. Y. Pui. An improved atomizer with high output of nanoparticles. *Journal of Aerosol Science*, 124:10–16, 2018.

[34] G. Taylor. Generation of ripples by wind blowing over a viscous fluid. *The Scientific Papers of GI Taylor*, 3:244–254, 1940.

[35] C. M. Varga, J. C. Lasheras, and E. J. Hopfinger. Initial breakup of a small-diameter liquid jet by a high-speed gas stream. 2003.

[36] J. Whitlow and A. H. Lefebvre. Effervescent atomizer operation and spray characteristics. *Atomization and Sprays*, 3(2), 1993.

Appendix A

ImageJ

A.1 ImageJ Macro

The following macro code was used in ImageJ to process all the images in a given data set to extract droplet diameter using feature segmentation.

```
    run("Subtract Background...", "rolling=100 light");
run("Enhance Contrast...", "saturated=0.01 normalize");
setAutoThreshold("Default");
run("Threshold...");
setThreshold(0, 128);
setOption("BlackBackground", false);
run("Convert to Mask");
run("Despeckle");
run("Close-");
run("Fill Holes");
run("Analyze Particles...", "size=125-Infinity display exclude include summarize");
```

A.2 Imagej Documentation

- **Subtract Background** – Removes smooth continuous backgrounds from gels and other images. Based on the concept of the 'rolling ball' algorithm described in Sternberg Stanley, Biomedical image processing, IEEE Computer, Jan 1983).

Imagine that the 2D grayscale image has a third dimension (height) by the image value at every point in the image, creating a surface. A ball of given radius is rolled over the bottom side of this surface; the hull of the volume reachable by the ball is the background to be subtracted.

- **Rolling ball radius** – The radius of curvature of the paraboloid. As a rule of thumb, for 8-bit or RGB images it should be at least as large as the radius of the largest object in the image that is not part of the background. Larger values will also work unless the background of the image is too uneven. For 16-bit and 32-bit images with pixel value ranges different from 0–255, the radius should be inversely proportional to the pixel value range (e.g., for 16-bit images (pixel values 0–65535), typical values of the radius are around 0.2 to 5).

- **Enhance Contrast** – Enhances image contrast by using either histogram stretching or histogram equalization. Both methods are described in detail in the Hypermedia Image Processing Reference — Contrast Stretching and Histogram Equalization. This command does not alter pixel values as long as Normalize, Equalize Histogram or Normalize.

  Saturated Pixels : Determines the number of pixels in the image that are allowed to become saturated. Increasing this value will increase contrast. This value should be greater than zero to prevent a few outlying pixel from causing the histogram stretch to not work as intended.

  Normalize : If checked, ImageJ will recalculate the pixel values of the image so the range is equal to the maximum range for the data type, or 0–1.0 for float images. The contrast stretch performed on the image is similar to the 'Auto' option in the Brightness/Contrast window, except that with stacks, each slice in the stack is adjusted independently, according to the optimal for that slice alone (if Use Stack Histogram is unchecked).

- **AutoThreshold** – Uses the currently selected thresholding method to automatically set the threshold levels based on an analysis of the histogram of the current image or selection.

- **Black Background** – To be checked when features are lighter than the background. The state of the checkbox is remembered across restarts. atmosphere.

- **Convert to mask** – Converts an image to black and white. The mask will have an inverting LUT (white is 0 and black is 255) unless Black Background is checked in.

- **Despeckle** – This is a median filter. It replaces each pixel with the median value in its 3 x 3 neighborhood. This is a time consuming operation because, for each pixel in the selection, the nine pixels in the 3x3 neighborhood must be sorted and the center pixel replaced with the median value (the fifth). Median filters a good at removing salt and pepper noise.

- **Close** – Performs a dilation operation, followed by erosion. This smoothes objects and fills in small holes.

- **Analyse particles** – This command counts and measures objects in binary or thresholded images according to the parameters set with the Analyze–Set Measurements dialog.. It works by scanning the image or selection until it finds the edge of an object. It then outlines the object using the wand tool, measures it using the Measure command, fills it to make it invisible, then resumes scanning until it reaches the end of the image or selection. Particles outside the range specified in the Size field are ignored. Enter a single value in Size and particles smaller than that value are ignored. Particles with circularity values outside the range specified in the Circularity field are also ignored.A value of 1.0 indicates a perfect circle. Check Summarize to display, in a separate window, the particle count, total particle area, average particle size, and area fraction.

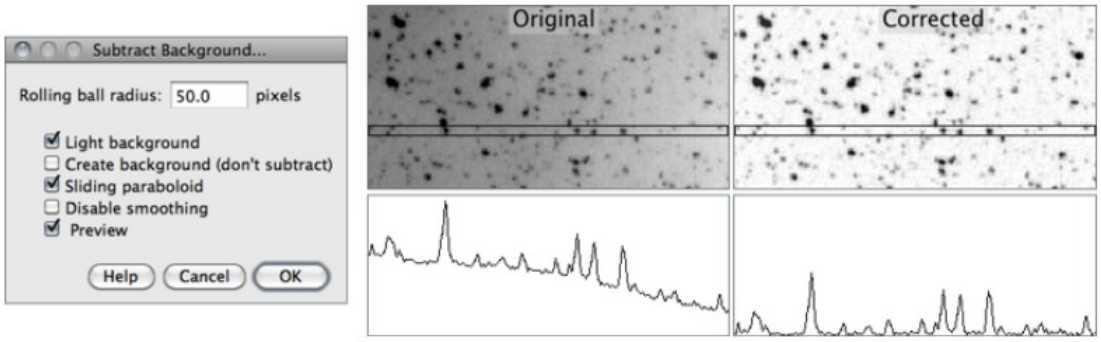

Figure A.1: Example of background correction using Imagej

Appendix B

Calibration Technique

In order to calibrate, the entire technique it was necessary to compare measured value to a known reference value to gauge the error in measurement. The data acquisition and image processing technique are calibrated using a glass slide. This slide was prepared at the Minnesota Nanofabrication Center (MNC).

Figure B.1: Slide used for calibrating the experimental technique used in this study

The slide shown in Fig B.1 was placed on the plane of focus for the long distance microscope. Raw images were captured for a sample dot size of 150 microns. Next, using the Imagej macro described in the previous section , the raw image was processed to extract information on the dot size. A head to head comparison has been shown in fig B.2.

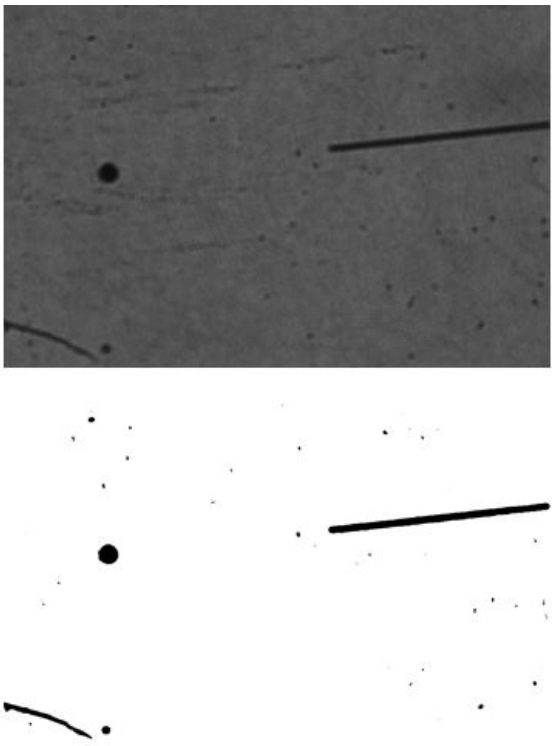

Figure B.2: (a) Raw Image (b) Processed Image for 0.15mm dot on the calibration slide

It is noted that the processed dot size had a diameter of 154.1 microns which is within 3 % of the actual size on the slide.

Appendix C

Nozzle Configuration

The experimental setup has been developed in a modular fashion so as to explore a range of different liquid tube & endcap dimensions. Influence of geometric parameters on the spray quality has been kept outside of the scope of present work. Table C.1 & Table C.2 presents a overview of different nozzle configurations that have been machined at the Machine shop at University of Minnesota. ID of Liquid Tube refers to d2 whereas OD & ID of endcap refer to d1 & d0 dimensions as shown in Fig 4.2 .

Sr.No	OD Measured (mm)	ID Measure (mm)
A	3.15	1.58
B	3.40	2.67
C	3.18	1.8
D	3.05	2.52
E	4.27	2.16
F	3.76	3.05

Table C.1: Liquid Tube Dimensions

Sr.No	OD Measured (mm)	ID Measure (mm)
1	0.99	0.58
2	2.08	1.55
3	3.05	2.54
4	1.04	0.56
5	2.24	1.75
6	1.27	0.81
7	Flow Blurring	2.51
8	1.27	0.84
9	Flow Blurring	1.58

Table C.2: End cap Dimensions